Monthly Notices
of the
ROYAL ASTRONOMICAL SOCIETY

MNRAS **494,** 5682–5703 (2020)
Advance Access publication 2020 April 24

doi:10.1093/mnras/staa1107

A magnetic snapshot survey of F-type stars

J. M. Seach,[1]★ S. C. Marsden,[1] B. D. Carter,[1] C. Neiner,[2] C. P. Folsom,[3] M. W. Mengel,[1] M. E. Oksala[2,4] and B. Buysschaert[2,5]

[1]*University of Southern Queensland, Centre for Astrophysics, Toowoomba 4350, Australia*
[2]*LESIA, Paris Observatory, PSL University, CNRS, Sorbonne University, Université de Paris, 5 place Jules Janssen, F-92195 Meudon, France*
[3]*IRAP, Université Toulouse, CNRS, CNES, UPS, F-31400 Toulouse, France*
[4]*Department of Physics, California Lutheran University, 60 West Olsen Road # 3700, Thousand Oaks, CA 91360, USA*
[5]*Instituut voor Sterrenkunde, KU Leuven, Celestijnenlaan 200D, B-3001 Leuven, Belgium*

Accepted 2020 April 20. Received 2020 April 18; in original form 2019 November 20

ABSTRACT

We present a spectropolarimetric magnetic snapshot survey of 55 stars which includes 53 F-type stars ranging from spectral types F0 to F9 plus 2 chemically peculiar stars β CrB, and δ Cap. We look for magnetic fields in stars spanning a range of effective temperatures where the transition from fossil to dynamo magnetic fields is believed to occur. High-resolution spectropolarimetry using circularly polarized spectra is used to look for a magnetic detection in the Stokes V profile, determine the mean longitudinal magnetic field (B_l), and to look for correlations with stellar parameters. Surface magnetic fields are detected on 14 F-stars, and present in every spectral class from F3V-F9V ranging in strength from 0.3 ± 0.1 G (36 UMa, F8V) to 8.3 ± 0.9 G (h Dra, F8V). Thus we find photospheric magnetic fields are present in stars as early as spectral type F3V with an outer convection zone thickness less than a few per cent of the stellar radius.

Key words: stars: early-type – stars: late-type – stars: magnetic field.

1 INTRODUCTION

Magnetic fields are present almost everywhere in the Universe and span 26 orders of magnitude from the extragalactic medium 10^{-9} G (Dolag et al. 2010) to the interior of magnetars 10^{17} G (Beskin et al. 2016). The Sun was first shown to be magnetic by Hale (1908) who identified the existence of a strong magnetic field in sunspots. The second magnetic star (78 Vir, A2p) was not discovered for another 40 yr, with the pioneering paper by Babcock (1947) who developed a technique for measuring stellar magnetic fields using circular polarization. Recent advances in spectropolarimetry enabled by the high resolution instruments ESPaDOnS (CFHT, Hawaii) (Donati 2003; Donati et al. 2006a), and NARVAL (Pic du Midi Observatory, France) (Aurière 2003) have enabled sub-Gauss stellar magnetic fields to be detected for the first time (Lignières et al. 2009). This has opened up new opportunities for understanding the nature of stellar magnetic fields across a range of masses, as shown for example by the MiMeS survey of hot stars (Wade et al. 2016) and the BCool survey of solar-type stars (Marsden et al. 2014).

F-type stars occupy an interesting region on the Hertzsprung-Russell diagram where important changes occur in the stellar atmosphere. They occupy a 'sweet spot' (Mizusawa et al. 2012) spanning a region where warm stars with negligible outer convection zones and fossil magnetic fields, transition to cool stars with deepening outer convection zones and dynamo magnetic fields. Fossil magnetic fields (Cowling 1945; Spitzer 1958; Mestel 1967; Neiner et al. 2015; Braithwaite & Spruit 2017) may originate from several different sources including primordial fields retained from the molecular cloud from which the stars were formed (Mestel & Spitzer 1956; Mestel 1966), from pre-main sequence dynamos (Moss 2001), or stellar mergers (Shultz et al. 2019). These fossil fields decay over a time-scale of the order of the lifetime of the star (Cowling 1945) and are frozen (Schussler 1975) into the atmosphere. Fossil magnetic fields are only detected in up to 10 per cent of hot stars (Grunhut et al. 2017; Sikora et al. 2018), and their strengths peak at 34 kG (Babcock 1960). In contrast, cool stars host dynamo generated magnetic fields (Moffatt 1978; Parker 1979; Krause & Radler 1980; Zeldovich, Ruzmaikin & Sokolov 1983; Roberts & Soward 1992; Brandenburg & Subramanian 2005; Mestel 2012) which show complex and dynamic structures.

The location of the transition between fossil and dynamo magnetic fields is believed to occur somewhere from early-to-mid F-stars, based on activity-rotation relationships (Wilson 1966), stellar wind breaking (Schatzman 1962; Kraft 1967; Skumanich 1972; Böhm-Vitense & Dettmann 1980), coronal X-ray emission (Schmitt et al. 1985), and mixing-length theory (Demarque & Roeder 1967; Baschek & Reimers 1969). Studying the transition from fossil to dynamo magnetic fields in F-stars is important for understanding the nature of the stellar dynamo, and dynamics of the outer atmospheres

★ E-mail: john.seach@usq.edu.au

of stars. The photospheric magnetic field is also an important input parameter for models of stellar winds surrounding F-stars, which affects the heliospheric magnetic field (Owens & Forsyth 2013) in the environment at the hot end of habitability for exoplanets (Sato et al. 2014).

The aim of this paper is to use high-resolution spectropolarimetry of a sample ranging from early-to-late F-type stars to determine the strength of the longitudinal magnetic field (B_l), and look for correlations with stellar parameters. This provides an insight into the nature of magnetism in stars with thin outer convection zones.

2 OBSERVATIONS

2.1 Target selection

Our 55 targets (Table 1) consist of 25 stars chosen as part of our transition project ranging from spectral type F2-F9, and 30 stars from the BRITEpol project (Neiner et al. 2017a) with 28 stars ranging from spectral type F0-F9, plus the chemically peculiar stars β CrB (Han et al. 2018) and δ Cap (Gray et al. 2006). δ Cap is classified as an Am star (Trilling et al. 2007) and these stars are expected to show only weak or non-existent magnetic fields (Conti 1970; Trust et al. 2020). The BRITEpol stars helped expand our sample mainly for early F-stars. Targets are chosen to be bright enough ($\leq$ mag 5) to enable a high signal-to-noise ratio (SNR) to be achieved with a reasonable exposure time. The sample was also limited by time allocated at the telescope and weather conditions. Table 2 shows our sample of 53 F-stars (excluding two chemically peculiar stars β CrB and δ Cap) consists of 27 per cent of the F-stars $\leq$ mag 5 from the Bright Star Catalogue (Hoffleit 1991). The proportion of our F-stars stars in each spectral type ranges from 12 to 56 per cent, indicating good coverage from each spectral class. A journal of observations for our stars are shown in Table 3. Further details for the individual transition project stars are found in Appendix A. Background information on the 30 BRITEpol stars used in this paper can be found in Marsden et al. (in preparation).

2.2 Spectropolarimetry

Observations of our 55 stars were obtained with both Stokes *I* (unpolarized) and Stokes *V* (circular polarized) light using the 3.6 m Canada-France-Hawaii Telescope (CFHT; Mauna Kea, Hawaii, with ESPaDOnS spectropolarimeter), the 2.0 m Télescope Bernard Lyot, (TBL, Observatoire du Pic du Midi, France, with NARVAL spectropolarimeter), and 3.6 m European Southern Observatory telescope (La Silla Observatory, Chile, using HARPSpol polarimetric mode of the HARPS spectrograph).

The ESPaDOnS (Aurière 2003) and NARVAL (Donati et al. 2006a) spectropolarimeters are almost identical instruments. They consist of a cross-dispersed, bench mounted, echelle spectrograph and a Cassegrain unit. Both NARVAL and ESPaDOnS have a spectrograph wavelength coverage in a single exposure from 370–1050 nm with small gaps at 922.4–923.4 nm, 960.8–963.6 nm, and 1002.6–1007.4 nm. The full spectrum spans 40 grating orders from #22 in the red to #61 in the blue, with a resolving power of $\approx$ 68 000 when using the spectropolarimetric mode. The Cassegrain module consists of the polarimeter, calibration unit and guiding camera, and has a 1.6 arcsec aperture.

The HARPSpol spectropolarimeter (Snik et al. 2008; Piskunov et al. 2011) is a bench-mounted spectrograph, fibre fed from the Cassegrain unit which contains the polarimetric optics. The wavelength coverage is from 380–690 nm with gaps between 526 and 534 nm, and a resolving power of $\approx$ 110 000. The spectra are recorded on two 2k $\times$ 4k EEV CCD's, with the full spectrum spanning 71 orders with 45 on the blue CCD and 26 on the red CCD.

2.3 Extraction of spectra

The extraction and calibration of polarized spectra from ESPaDOnS and NARVAL were completed automatically using the libre-ESpRIT software package based on an algorithm by Donati et al. (1997). The HARPSpol data were reduced using the REDUCE package (Piskunov & Valenti 2002; Makaganiuk et al. 2011). The output of libre-ESpRIT and REDUCE are intensity spectra (Stokes *I*), circular polarization (Stokes *V*), and null (*N*) polarization spectra. One stellar observation consists of four sub-exposures which are combined to produce the Stokes *I*, combined constructively to produce the Stokes *V* spectrum, and combined destructively to give the null spectrum where the Zeeman signature cancels out, leaving only non-magnetic effects in the profile (Semel, Donati & Rees 1993; Donati et al. 1997; Bagnulo et al. 2012). This acts as a check to ensure spurious signatures have not contaminated the circular polarization spectra.

3 DATA ANALYSIS

3.1 Least-Squares Deconvolution (LSD)

The magnetic fields of F-stars are expected to be weak (Marsden et al. 2014), and difficult to detect above background noise. Our data analysis involves combining the contribution of many spectral lines to give a mean line with higher SNR which improves the sensitivity of magnetic field detection (Semel 1989; Semel & Li 1996). We use the line addition technique of Least Squares Deconvolution (LSD) (Donati et al. 1997, 2006b) to improve the ability to detect a magnetic signal. LSD combines thousands of spectral lines into a single line with mean parameters. The method is based on the assumption that the circular polarization line profiles across different wavelengths correspond to a common basic Zeeman signature (Semel et al. 2009). The LSD profiles are generated from line masks which are created using the Vienna Atomic Line Database (VALD3) (Ryabchikova et al. 2015). Effective temperature, surface gravity, and metallicity are used as inputs and lines are chosen with a depth greater than or equal to 10 per cent of the continuum. The line mask which best matches each star are from Marsden et al. (2014). The sampling size for LSD output velocity bins are chosen as 1.8 km s^{-1}.

The number of lines used in the LSD calculation varies from 6192 to 18879 (Table 4). A larger number of lines are used for spectra obtained with NARVAL, which accounts for most of our hotter stars. This may have been due to overlap with the orders on NARVAL, with many lines being counted twice. The weighting of spectral lines are adjusted as in Marsden et al. (2014) to produce a mean weight of the Stokes *I* and *V* LSD profiles close to unity. The normalization parameters from Marsden et al. (2014) are used, varying every 250 K up to a maximum of 6500 K and extrapolated for temperatures above this. Extrapolation of the normalization parameters for our hotter stars is considered reasonable since the values only changed a small amount with increasing effective temperature. In addition to combining multiple lines to produce a LSD profile, we also co-added individual LSD profiles from a single night to give a mean value with even higher sensitivity. The SNR of our mean LSD profiles shown in (Table 4) are generally higher (by a factor of 2–3 times)

Table 1. Stellar parameters for our 55 stars.

Target	HIP	Spectral Type	$T_{\rm eff}$ (K)	Age (Gyr)	$v\sin i$ (km s^{-1})	Refs[2] (s,t,a,v)
F-star definite detections						
β CrB	75695	*	7980 ± 180	0.6 ± 0.3	13.7 ± 6.1	*, 5, 5, 3
σ Boo	71284	F3V	6720 ± 144	1.6 ± 0.3	9.7 ± 2.3	16, 1, 2, 3
ϵ Lib	75379	F4V+K5-M2	6405 ± 187	2.0 ± 0.1	9.5 ± 0.7	17, 1, 2, 3
ϵ Cet	12390	F5V+F6V	6537 ± 129[1]	2.4 ± 0.5	10.8 ± 5.5[1]	17, 1, 2, 3
α Com	64241	F5V+F6V	6433 ± 325[1]	2.9 ± 0.1	20.0 ± 6.1[1]	17, 5, 2, 3
χ Dra	89937	F7V+K1V	6150 ± 57	5.2 ± 0.6	5.1 ± 2.9	17, 9, 2, 3
h Dra	82860	F8V+M1V	6271 ± 80	2.3 ± 0.9	10.0 ± 0.5	17, 1, 2, 3
36 UMa	51459	F8V+K7	6183 ± 118	0.5 ± 1.4	6.0 ± 4.0	17, 1, 2, 3
17 Crt	56280	F8V+F8V	6157 ± 42[1]	2.8 ± 0.2	8.7 ± 0.5[1]	17, 1, 2, 3
γ CrA B	93825	F8V	6188 ± 80[1]	3.2 ± 1.1	8.4 ± 4.0[1]	17, 2, 2, 3
ω Dra B	86201	F8V	5900	2.1 ± 0.4	12.8 ± 2.8[1]	15, 15, 2, 3
θ Dra	78527	F8IV+M2	6105 ± 271	2.1 ± 0.2	28.1 ± 0.9	18, 1, 2, 3
β Vir	57757	F9V	6083 ± 58	3.1 ± 0.8	6.1 ± 2.6	17, 10, 2, 3
F-star marginal detections						
τ PsA	109422	F6V	6352 ± 36	0.6 ± 0.3	12.8 ± 0.8	17, 1, 2, 3
γ Ser	78072	F6V	6291 ± 50	3.1 ± 0.4	10.0 ± 0.7	17, 6, 2, 3
F-star non-detections						
δ Cap	107556	kA5hF0mF2III	7395 ± 251	2.8 ± 0.0	90.0 ± 2.4	22, 5, 12, 3
α Hyi	9236	F0IV	7377 ± 251	0.8 ± 0.4	135.3 ± 19.8	17, 5, 5, 3
h UMa	46733	F0IV+K5	7101 ± 241	1.5 ± 0.1	144.0 ± 2.9	17, 5, 2, 3
γ Cap	106985	F0III	7167 ± 206	1.5 ± 0.0	31.0 ± 10.0	19, 7, 11, 3
δ Ser	76276	F0IV+F0IV	6954 ± 371[1]	1.0 ± 0.0	88.0 ± 10.0[1]	16, 1, 11, 3
α Crv	59199	F1V	6722 ± 440	0.2 ± 0.6	24.9 ± 0.9	17, 1, 2, 3
β TrA	77952	F1V	7458 ± 254	0.9 ± 0.5	82.3 ± 6.1	17, 5, 5, 3
δ Aql	95501	F1IV-V	7216 ± 245	1.5 ± 0.0	85.1 ± 5.4	17, 5, 11, 3
ω Dra A	86201	F2V	6500	2.1 ± 0.4	12.8 ± 2.8[1]	15, 15, 2, 3
υ UMa	48319	F2IV+M	6738 ± 306	1.3 ± 0.0	105.7 ± 4.2	16, 1, 11, 3
δ Gem	35550	F2IV-V+K3	6300 ± 248	1.9 ± 0.1	121.7 ± 6.2	3, 1, 2, 3
τ Cyg	104887	F2IV+G0V	6772 ± 230	1.8 ± 0.0	88.4 ± 13.5	17, 5, 13, 3
η Lep	28103	F2V	6560 ± 311	1.8 ± 0.2	16.2 ± 1.1	17, 1, 2, 3
ι Leo	55642	F3V+G3V	6536 ± 415	1.5 ± 0.1	14.5 ± 2.1	17, 1, 2, 3
10 UMa	44248	F3V+G5V	6538 ± 222[1]	1.7 ± 0.5	21.4 ± 1.3[1]	17, 5, 2, 3
ψ Vel	46651	F3V+F0IV	7122 ± 242[1]	1.5 ± 0.1	260.0[1]	17, 5, 2, 3
γ Tuc	114996	F3IV/V	6561 ± 148	1.8 ± 0.2	84.8 ± 6.2	20, 1, 2, 3
γ Cet	12706	F4V+A2Vn	6982 ± 329[1]	0.6 ± 0.1	10.0[1]	17, 1, 8, 3
σ Cet	11783	F4IV+K5	6393 ± 53	2.5 ± 0.1	8.4 ± 5.5	3, 1, 2, 3
58 Oph	86736	F5V+G5	6351 ± 81	2.1 ± 0.6	12.8 ± 1.3	17, 1, 2, 3
β Del	101769	F5IV+F5IV	6485 ± 67[1]	1.5 ± 0.0	47.0 ± 4.8[1]	17, 1, 13, 3
ψ Gem	32362	F5IV-V	6510 ± 221	1.6 ± 0.1	68.3 ± 6.2	17, 5, 2, 3
α CMi	37279	F5IV-V+DQZ	6652 ± 226	1.7 ± 0.4	5.2 ± 2.1	17, 5, 2, 3
ι Peg	109176	F5V+G8V	6265 ± 380	1.7 ± 0.5	7.9 ± 2.5	17, 1, 2, 3
ψ Peg	112447	F6V+M1	6282 ± 238	3.2 ± 0.4	8.1 ± 1.0	17, 1, 2, 3
μ Cyg	107310	F6V+G2V	6406 ± 138	2.7 ± 0.3	7.3 ± 3.3	17, 1, 2, 3
α For	14879	F6V+G7V	6208 ± 248	3.2 ± 1.2	7.8 ± 4.3	17, 1, 2, 3
γ Lep	27072	F6V+K2	6333 ± 28	1.0 ± 1.1	9.9 ± 3.0	17, 2, 2, 3
θ UMa	46853	F6IV+M	6374 ± 50	2.3 ± 0.2	7.8 ± 1.6	3, 6, 2, 3
ι Psc	116771	F7V+M5	6186 ± 174	3.2 ± 0.2	6.6 ± 1.4	17, 1, 2, 3
σ02 UMa	45038	F7IV-V+K6	6315 ± 103	2.6 ± 0.3	7.3 ± 1.9	21, 1, 2, 3
δ Equ	104858	F7V+G0V	6283 ± 395[1]	3.0 ± 0.2	6.1 ± 1.1[1]	17, 1, 2, 3
γ Del	102531	F7V+K1 IV	6450 ± 91	2.1 ± 0.2	8.7 ± 4.5	3, 6, 2, 3
6 Cet	910	F8V	6258 ± 90	3.9 ± 1.1	5.8 ± 2.3	17, 1, 2, 3
ζ Cnc	40167	F8V+G0V	6191 ± 85[1]	2.6 ± 0.2	2.8 ± 0.5[1]	17, 2, 2, 3
γ CrA A	93825	F8V	6188 ± 80[1]	3.2 ± 1.1	8.4 ± 4.0[1]	17, 2, 2, 3
HD 84117	47592	F9V	6168 ± 283	2.6 ± 0.7	5.7 ± 0.5	17, 1, 2, 3
η Cas	3821	F9V+K5-M0	5801 ± 132	2.9 ± 7.2	3.9 ± 2.6	17, 14, 2, 3
Definite detections, but uncertain which component						
κ Peg	107354	F5IV+G0V	6581 ± 224[1]	1.3 ± 0.1	19.9 ± 9.3[1]	3, 5, 2, 3
20 Oph	82369	F6IV+>G2	6295 ± 66[1]	1.6 ± 0.3	10.3 ± 1.4[1]	22, 1, 2, 3

Notes. Parameters refer to the F-star component, unless marked with superscript[1] where the value is a combined value from binary components.

References: 1: Gaia collaboration (2018), 2: Casagrande et al. (2011), 3: Glebocki & Gnacinski (2005), 4: Anderson & Francis (2012), 5: David & Hillenbrand (2015), 6: Aguilera-Gómez, Ramírez & Chanamé (2018), 7: McDonald, Zijlstra & Watson (2017), 8: Gullikson, Kraus & Dodson-Robinson (2016), 9: Torres, Andersen & Giménez (2010), 10: Jofre et al. (2018), 11: Gontcharov (2012), 12: Vican (2012), 13: Marsakov & Shevelev (1995), 14: Prieto & Lambert (1999), 15: Konacki et al. (2010), 16: Samus et al. (2017), 17: Wenger et al. (2000), 18: Slovak & Barnes (2002), 19: Chen, Liu & Shan (2017), 20: Wright et al. (2003), 21: Edwards (1976), 22: Gray et al. (2006).

[2]The order of references in column 7 corresponds to spectral type (s), $T_{\rm eff}$ (t), age (a) and $v\sin i$ (v).

*No spectral type assigned to β CrB.

Table 2. Comparison of the 53 F-stars in our sample with the ≤ mag 5 F-stars from Bright Star Catalogue (Hoffleit 1991). Table does not include β CrB and δ Cap with no assigned spectral type.

Spectral Type	No. of F-stars in our sample	No. F-stars in BSC ≤ mag 5	Per cent sampled
F0	4	33	12
F1	3	6	50
F2	5	32	16
F3	5	14	36
F4	3	10	30
F5	8	29	28
F6	8	28	29
F7	5	13	38
F8	9	16	56
F9	3	12	25
Total	53	193	27

for the 25 transition project stars observed with CFHT compared to the 30 BRITEpol stars. The SNR of the mean Stokes *V* profiles are determined by propagating the formal error bars associated with each spectral pixel through the deconvolution (Wade et al. 2000). The time between the first and last exposure on each night typically covers less than 5 per cent of the star's estimated rotation period, thus minimising smearing of the magnetic field. The stellar rotation period is estimated using literature values of projected rotational velocity ($v \sin i$), stellar radius, and assuming an inclination of 60 degrees. LSD profiles for 15 stars with a magnetic detection are shown in Appendix B.

3.2 Longitudinal magnetic field (B_l)

The mean longitudinal magnetic field (B_l) is defined as the line of sight component of the magnetic field, averaged over the visible stellar disc (Babcock 1947; Schwarzschild 1950). According to Donati et al. (1997),

$$B_l = -2.14 \times 10^{11} \frac{\int v V(v) \mathrm{d}v}{\lambda g c \int [I_c - I(v)] \mathrm{d}v}, \quad (1)$$

where B_l is the longitudinal magnetic field in gauss, λ is the mean wavelength of LSD profile in nm, g is the mean value of the Landé factors of all lines used to construct the LSD profile, c is the speed of light (in the same units as v), and I_c is the continuum level of the intensity profile. B_l is measured from the first-order moment of the Stokes *V* LSD profile (Donati et al. 1997; Wade et al. 2000), and as a first approximation is proportional to the shift in wavelength between left and right circular polarization lines (Mathys 1995). The mean wavelength and Landé factors are the same as normalization parameters discussed in 3.1. The error in B_l is calculated by propagating the uncertainties in the reduction pipeline through equation (1).

B_l is a widely used measure of stellar magnetic fields in both hot (Wade et al. 2016) and cool stars (Marsden et al. 2014), although its use is subject to several limitations. Since B_l is averaged over the visible stellar hemisphere and therefore, the entire width of the line profile, it may give a null result due to cancellation effects where areas of opposite polarity cancel out, even if a magnetic field is present in individual LSD velocity bins. B_l is a measure of the large-scale magnetic field and therefore not sensitive to small-scale fields, which means that a large part of the surface flux may be missed (Reiners & Basri 2009). Our snapshot survey determines B_l at one particular point of the rotational phase. Therefore, our determined B_l is the maximum field strength at the time of observation, and may be different if measured at another rotational phase.

3.3 Magnetic field detection

A second method for determining the presence of a magnetic field on the surface of stars is the False Alarm Probability (FAP), which is a statistical criteria used to determine if a star has either a magnetic signature in the Stokes *V* or a spurious signal in the Null profile (Donati, Semel & Rees 1992; Donati et al. 1997). The technique uses chi-square (χ^2) statistics which are computed inside and outside the spectral line using the probability function of Abramowitz & Stegun (1964), which is then converted into a detection probability. χ^2 statistics are used outside stellar lines to check any magnetic detection is stellar in origin, and not from spurious sources which may show as a detection outside the lines. The χ^2 probability function according to Donati et al. (1992) is used to give the probability of the circularly polarized data deviating from a zero magnetic field. A magnetic signal is considered unambiguously detected if the FAP is smaller than 10^{-5}, a marginal detection if FAP between 10^{-3} and 10^{-5}, and no detection if FAP is greater than 10^{-3}. A magnetic detection requires no detection of signal outside the spectral line nor in the null profile.

Integration limits for determination of the FAP were estimated visually from the LSD Stokes *I* profile, centred on the line core and covering the full profile up to the continuum on the red and blue wings. The integration limits were chosen to be wide enough to include information in the Stokes *V* profile, but narrow enough to minimize noise from outside the profile. An analysis by Wade et al. (2000) showed that even though integration limits are somewhat subjective, the FAP is relatively insensitive to small variations. Determination of FAP was done for both the Stokes *V* and null profiles.

A detection of signal in the Stokes *V* can be the result of true polarization caused by a photospheric magnetic field, or a spurious signal caused by instrumental or other effects. The stellar origin of the polarization signal is confirmed by checking the signal is located only in the Stokes *V* profile and not located in the Null profile, and that the signal is located within the line velocity range (Donati et al. 1997). FAP for our stars are listed in Table 4.

3.4 Spectral line analysis

3.4.1 Radial velocity

The stellar radial velocity (Lindegren & Dravins 2003) is the line of sight component of a star's motion and is a basic stellar parameter. The radial velocity of our stars (Table 5) are computed by using the centre of gravity (COG) method (Uitenbroek 2003). The radial velocities derived in this work are compared to literature values of Buccino & Mauas (2008), Anderson & Francis (2012), and are used as an input into the S-index calculation (Section 3.5), and as a reference for analysing line asymmetries in the Stokes *I* profiles (Section 3.4.2). Radial velocities for our stars are calculated from the mean and standard deviation from individual measurements on the night of maximum B_l determination. The radial velocity precision of ESPaDOnS is about 15 m s^{-1} within a single run and 30 m s^{-1} from run to run (Moutou et al. 2007), where a run comprises observations over several consecutive nights. The radial velocity precision of NARVAL is 18 m s^{-1} and HARPS 0.7 m s^{-1} (Soubiran et al. 2018).

Table 3. Journal of observations for our 55 stars showing dates corresponding to maximum B_l determination.

Target Star	Instrument	HJD Range 2450000+	Date YMD	UT HMS	T_{exp} (s)	SNR Range (Stokes *I*)
F-star definite detections						
β CrB	NARVAL	7867.579	2017-04-23	01:42:18	4 × 150	968
σ Boo	ESPaDOnS	7768.051–7768.158	2017-01-14	13:15:45–15:50:15	4 × 139	648–727
ϵ Lib	ESPaDOnS	7826.005–7826.149	2017-03-13	12:02:24–15:29:10	4 × 113	666–706
ϵ Cet	ESPaDOnS	7652.916–7653.174	2016-09-21	09:53:06–16:05:07	4 × 199	629–737
α Com	ESPaDOnS	7800.910–7801.083	2017-02-16	09:45:45–13:55:44	4 × 120	757–849
χ Dra	NARVAL	7136.582	2015-04-24	01:54:01	4 × 120	780
h Dra	ESPaDOnS	7882.876–7883.028	2017-05-09	08:59:56–12:39:36	4 × 194	645–716
36 UMa	ESPaDOnS	7767.055–7767.166	2017-01-13	13:16:37–15:57:38	4 × 180	690–704
17 Crt	ESPaDOnS	7817.859–7818.043	2017-03-05	08:28:37–12:52:52	4 × 209	600–680
γ CrA B	ESPaDOnS	7910.958–7911.022	2017-06-06	10:54:23–12:25:43	4 × 101	553–617
ω Dra B	ESPaDOnS	7878.921–7879.070	2017-05-05	10: 05:44–13:40:13	4 × 189	761–785
θ Dra	NARVAL	7889.433–7889.504	2017-05-15	22:09:39–23:51:32	4 × 320	726–1018
β Vir	NARVAL	7855.453–7855.466	2017-04-11	22:39:39, 22:54:36	4 × 223	894–1024
F-star marginal detections						
τ PsA	ESPaDOnS	7676.742–7676.925	2016-10-15	05:46:08–10:08:44	4 × 204	740–849
γ Ser	NARVAL	6893.329–6893.344	2014-08-23	19:43:51–20:06:05	4 × 269	488–491
F-star non-detections						
δ Cap	NARVAL	6950.367–6950.396	2014-10-19	20:40:22–21:21:21	4 × 103	348–420
α Hyi	HARPSpol	6969.641–6969.677	2014-11-08	03:16:44–04:07:51	4 × 120	885–891
h UMa	NARVAL	6643.622	2013-12-17	02:41:11	4 × 234	378
γ Cap	NARVAL	6912.404	2014-09-11	21:30:08	4 × 95	338
δ Ser	NARVAL	6764.633–6764.661	2014-04-17	02:54:42–03:35:05	4 × 239	353–357
α Crv	ESPaDOnS	6694.089–6694.132	2014-02-05	14:00:41–15:03:43	4 × 50	513–524
β TrA	HARPSpol	7481.744–7481.7573	2016-04-03	05:44:21–06:02:53	4 × 106	944–955
δ Aql	NARVAL	6811.623–6811.635	2014-06-03	02:43:02–03:00:12	4 × 194	353–358
ω Dra A	ESPaDOnS	7878.921–7879.070	2017-05-05	10: 05:44–13:40:13	4 × 189	761–785
υ UMa	NARVAL	6764.376–6764.406	2014-04-16	20:50:24–21:33:35	4 × 260	352–361
δ Gem	NARVAL	7134.325–7134.372	2015-04-21	19:41:44–20:49:56	4 × 190	347–361
τ Cyg	NARVAL	6816.586–6816.615	2014-06-08	01:53:00–02:34:52	4 × 250	392–396
η Lep	NARVAL	7327.718	2015-11-01	05:00:03	4 × 95	330
ι Leo	NARVAL	7800.534–7800.598	2017-02-16	00:29:31–02:02:09	4 × 286	498–506
10 UMa	ESPaDOnS	7745.011–7745.144	2016-12-22	12:11:25–15:23:12	4 × 105	797–827
ψ Vel	ESPaDOnS	6699.918–6699.954	2014-02-11	09:54:15–10:46:28	4 × 60	629–653
γ Tuc	HARPSpol	7235.793–7235.817	2015-08-01	06:48:46–07:23:02	4 × 224	1313–1317
γ Cet	NARVAL	6947.567–6947.642	2014-10-17	01:19:27–03:08:24	4 × 208	314–316
σ Cet	ESPaDOnS	7651.995–7652.055	2016-09-20	11:47:04–13:13:55	4 × 179	734–747
58 Oph	ESPaDOnS	7885.916–7886.040	2017-05-12	09:51:35–12:51:03	4 × 200	693–742
β Del	NARVAL	6786.650	2014-05-09	03:31:36	4 × 103	483
ψ Gem	NARVAL	6744.324–6744.345	2014-03-27	19:38:06–20:08:54	4 × 167	497–509
α CMi	NARVAL	7339.723	2015-11-13	05:16:21	4 × 10	1031
ι Peg	NARVAL	7623.528	2016-08-23	00:24:14	4 × 258	864
ψ Peg	ESPaDOnS	7615.860–7615.920	2016-08-15	08:30:08–09:55:56	4 × 105	715–732
μ Cyg	ESPaDOnS	7612.920–7613.035	2016-08-12	09:56:24–12:42:44	4 × 139	700–722
α For	ESPaDOnS	6703.707–6703.718	2014-02-15	04:58:05–05:13:23	4 × 50	51–411
γ Lep	ESPaDOnS	6698.811–6698.835	2014-02-10	07:22:17–07:55:58	4 × 53	683–704
θ UMa	NARVAL	7718.690–7718.745	2016-11-26	04:24:41–05:44:15	4 × 150	502–520
ι Psc	ESPaDOnS	7617.076–7617.156	2018-08-16	13:41:49–15:37:51	4 × 95	706–723
σ02 UMa	ESPaDOnS	7744.090–7745.172	2016-12-21	14:07:31–16:05:55	4 × 179	700–720
δ Equ	ESPaDOnS	7911.029–7911.125	2017-06-06	12:38:26–14:57:14	4 × 144	608–765
γ Del	NARVAL	6902.463–6902.479	2014-09-01	22:49:17–23:12:36	4 × 286	385–387
6 Cet	ESPaDOnS	7975.977–7976.017	2017-08-10	11:21:15–12:18:44	4 × 192	735–765
ζ Cnc	ESPaDOnS	7799.947–7799.964	2017-02-15	10:37:30–11:01:44	4 × 159	635–651
γ CrA A	ESPaDOnS	7911.967–7912.042	2017-06-07	11:06:00–12:54:50	4 × 101	564–620
HD 84117	ESPaDOnS	7823.910–7823.952	2017-03-11	9:42:01–10:42:42	4 × 201	691–705
η Cas	NARVAL	6902.580–6902.591	2014-09-02	01:45:18–02:01:24	4 × 177	481–482
Definite detections, but uncertain which component						
κ Peg	ESPaDOnS	7616.849–7617.068	2019-08-16	08:14:11–13:29:20	4 × 104	696–777
20 Oph	ESPaDOnS	7608.735–7608.862	2016-08-08	05:36:03–08:38:40	4 × 155	690–719

Table 4. Results from Stokes *V* LSD analysis our 55 stars.

Target Star	Obs. Date UT	T_{exp} (s)	No. Spectra[1]	SNR Stokes *V* mean LSD	No. lines used	FAP inside line	Vel range (km s^{-1})	B_l (G)	N_l (G)
F-star definite detections									
β CrB	23apr17	150.0	1	2766	17620	$<10^{-16}$	−31, −4	+735.8 ± 6.2	+0.1 ± 0.5
σ Boo	14jan17	139.0	14	105 071	6304	3.465×10^{-6}	−14, +16	− 1.4 ± 0.4	+0.5 ± 0.4
ϵ Lib	13mar17	213.0	14	114 485	6829	1.666×10^{-7}	−35, +10	− 0.5 ± 0.1	+0.1 ± 0.1
ϵ Cet	21sep16	199.0	16	124 397	6693	1.456×10^{-11}	−5, +40	+0.6 ± 0.1	0.0 ± 0.1
α Com	16feb17	120.0	27	154 986	7628	$<10^{-16}$	−50, +20	+3.1 ± 0.3	+0.2 ± 0.4
χ Dra	24apr15	120.0	1	27 693	6838	$<10^{-16}$	+27, +61	− 6.3 ± 1.2	− 0.0 ± 1.2
h Dra	09may17	194.0	16	109 211	7186	$<10^{-16}$	−50, −15	+8.3 ± 0.9	+0.6 ± 0.9
36 UMa	13jan17	180.0	12	120 020	7058	$<10^{-16}$	−5, +25	− 0.3 ± 0.1	0.0 ± 0.1
17 Crt	5mar17	209.0	18	108 986	8309	4.441×10^{-16}	−10, +22	+0.4 ± 0.1	+0.2 ± 0.1
γ CrA B	06jun17	101.0	12	67 072	7608	$<10^{-16}$	−65, −40	+5.6 ± 0.8	− 0.2 ± 0.8
ω Dra B	05may17	189.0	16	135 380	9099	$<10^{-16}$	+15, +45	− 2.9 ± 1.2	− 1.0 ± 1.2
θ Dra	15may17	320.0	4	44 295	9552	8.203×10^{-13}	−50, +20	+7.4 ± 2.9	− 0.6 ± 2.9
β Vir	11apr17	223.0	2	48 830	10621	$<10^{-16}$	−14, +23	+1.7 ± 0.5	− 0.4 ± 0.5
F-star marginal detections									
τ PsA	15oct16	204.0	14	134 948	8637	2.233×10^{-5}	−40, +5	− 0.6 ± 0.2	+0.3 ± 0.2
γ Ser	23aug14	269.0	2	57 763	7265	6.800×10^{-3}	−10, +25	+0.9 ± 0.4	− 0.5 ± 0.4
F-star non-detections[2]									
δ Cap	19oct14	103.0	5	33 776	15411	4.896×10^{-1}	−120, +60	− 2.9 ± 5.9	1.4 ± 5.9
α Hyi	08nov14	120.0	6	32 272	15846	$1.000 \times 10^{+00}$	−150, +200	+24.8 ± 11.3	− 6.7 ± 11.3
h UMa	17dec13	234.0	1	22 999	16569	9.265×10^{-1}	−158, +151	− 3.8 ± 17.6	+21.3 ± 17.6
γ Cap	11sep14	95.0	1	14 394	16578	5.142×10^{-1}	−80, +10	+4.0 ± 3.6	+3.2 ± 3.6
δ Ser	17apr14	239.0	3	43 993	18879	9.863×10^{-1}	−160, +60	− 1.6 ± 4.8	+2.3 ± 4.9
α Crv	05feb14	50.0	8	42 414	16310	6.433×10^{-1}	−30, +40	− 0.8 ± 1.0	1.4 ± 1.0
β TrA	03apr16	106.0	3	27 157	14537	9.452×10^{-1}	−80, +80	− 17.3 ± 7.4	− 6.0 ± 7.4
δ Aql	03jun14	194.0	2	45 176	15389	7.127×10^{-1}	−120, +80	+3.3 ± 4.0	− 1.7 ± 4.1
ω Dra A	05may17	189.0	16	136 494	9096	3.358×10^{-1}	−65, −30	+0.2 ± 0.1	− 0.1 ± 0.1
υ UMa	16apr14	260.0	3	48 900	15291	9.831×10^{-1}	−90, +160	+2.6 ± 6.1	− 0.8 ± 6.4
δ Gem	21apr15	190.0	5	43 796	15241	9.056×10^{-1}	−140, +120	+20.8 ± 9.9	− 18.5 ± 9.9
τ Cyg	08jun14	250.0	3	45 303	16891	7.501×10^{-1}	−40, −10	− 3.6 ± 4.9	− 3.1 ± 4.9
η Lep	01nov15	95.0	1	13 989	15037	1.775×10^{-1}	−30, +30	− 6.6 ± 3.4	− 2.3 ± 3.4
ι Leo	16feb17	286.0	5	67 120	7507	7.171×10^{-1}	−40, +20	− 0.8 ± 0.4	0.0 ± 0.4
10 UMa	22dec16	105.0	21	189 946	8930	[3] $< 10^{-16}$	0, +60	[3] − 4.8 ± 1.1	+0.3 ± 1.1
ψ Vel	11feb14	60.0	9	47 467	16064	7.119×10^{-1}	−20, +30	− 3.3 ± 3.0	+1.8 ± 3.0
γ Tuc	01aug15	224.0	3	37 707	6192	6.996×10^{-1}	−100, +90	− 6.3 ± 6.2	− 2.1 ± 6.2
γ Cet	17oct14	208.0	7	59 547	16047	8.546×10^{-1}	−25, +5	− 45.2 ± 23.9	− 4.5 ± 23.9
σ Cet	20sep16	179.0	7	87 618	7482	5.724×10^{-1}	−50, −15	0.0 ± 0.2	0.0 ± 0.2
58 Oph	12may17	200.0	13	96 046	6833	9.002×10^{-1}	−15, +30	+0.4 ± 0.2	− 0.6 ± 0.2
β Del	09may14	103.0	1	28 969	8030	2.959×10^{-1}	−80, −20	− 3.1 ± 3.9	− 0.6 ± 4.0
ψ Gem	27mar14	167.0	3	64 315	7456	2.318×10^{-1}	−40, +100	− 5.1 ± 2.4	+2.9 ± 2.4
α CMi	13nov15	10.0	1	26 419	7468	7.746×10^{-1}	−20, +9	− 0.7 ± 0.3	− 0.3 ± 0.3
ι Peg	23aug16	258.0	1	28 229	6463	5.910×10^{-1}	−36, −18	− 3.6 ± 1.3	− 0.8 ± 1.3
ψ Peg	15aug16	105.0	10	109 945	7499	8.099×10^{-1}	−25, +15	+0.1 ± 0.1	0.0 ± 0.1
μ Cyg	12aug16	139.0	15	118 196	7043	2.649×10^{-1}	−2, +25	− 0.4 ± 0.1	0.0 ± 0.1
α For	15feb14	50.0	3	17 152	7152	8.189×10^{-1}	−30, +0	+3.1 ± 1.3	+0.3 ± 1.3
γ Lep	10feb14	63.0	6	75 580	8161	8.943×10^{-1}	−20, +10	− 0.2 ± 0.2	+0.2 ± 0.2
θ UMa	26nov16	150.0	7	66 879	7268	1.943×10^{-1}	0.0, +30	− 0.1 ± 0.2	+0.2 ± 0.2
ι Psc	16aug16	95.0	14	122 548	7502	4.510×10^{-3}	−15, +25	− 0.2 ± 0.1	+0.1 ± 0.1
σ02 UMa	21dec16	179.0	4	94 164	8648	9.598×10^{-1}	−20, +15	+0.1 ± 0.1	0.0 ± 0.1
δ Equ	06jun17	144.0	12	98 789	7182	2.012×10^{-2}	−40, +5	+0.7 ± 0.2	− 0.3 ± 0.2
γ Del	01sep14	286.0	2	64 651	10137	7.083×10^{-1}	−10, +5	− 0.1 ± 0.1	0.0 ± 0.1
6 Cet	10aug17	192.0	5	72 919	7659	4.349×10^{-1}	−2, +28	0.0 ± 0.1	+0.1 ± 0.1
ζ Cnc	15feb17	159.0	3	35 867	8813	6.533×10^{-1}	−20, +10	− 0.7 ± 0.4	− 0.1 ± 0.4
γ CrA A	07jun17	101.0	14	57 601	7613	6.317×10^{-1}	−70, −35	− 0.1 ± 0.1	− 0.1 ± 0.1
HD 84117	11mar17	201.0	5	69 158	8804	3.329×10^{-1}	+15, +50	+0.2 ± 0.1	+0.2 ± 0.1
η Cas	02sep14	177.0	2	58 444	7579	4.934×10^{-1}	−10, +10	0.0 ± 0.1	+0.1 ± 0.1
Definite detections, but uncertain which component									
κ Peg	16aug16	104.0	34	183 631	6684	3.757×10^{-13}	−50, −5	+0.9 ± 0.3	0.0 ± 0.3
20 Oph	08aug16	155.0	15	128 114	8378	2.612×10^{-6}	−20, +20	+0.7 ± 0.2	0.0 ± 0.2

Notes. [1]Spectra are constructed from four sub-exposures as described in Section 2.3. For example, the 14 spectra for σ Boo were produced from 56 sub-exposures. SNR for the Stokes *I* profiles are shown in Table 3.

[2]For stars with non-detections we have taken the maximum B_l measurement, and B_l values refer to an upper limit.

[3]Detection is most likely from the G-star component of the blended spectra.

Table 5. Radial Velocity (RV), S-index, bisector analysis, and Stokes *V* for our stars.

Target	RV this work (km s^{-1})	RV literature (km s^{-1})	S-index this work	S-index literature	Bisector slope	Bisector span (m s^{-1})	Stokes *V* Amplitude (*V*/*Ic*)
F-star definite detections							
β CrB	− 17.32 ± 0.07	− 26.90 ± 0.20	NA	NA	\	231 ± 13	–
σ Boo	+0.28 ± 0.01	+0.37 ± 0.09	0.240 ± 0.004	0.156–0.253	/	211 ± 35	0.059
ϵ Lib	− 13.98 ± 0.01	− 9.8 ± 0.70	0.180 ± 0.012	NA	\	13 ± 13	0.057
ϵ Cet	+15.81 ± 0.26	+15.49 ± 0.19	0.186 ± 0.003	0.219	NA	NA	NA
α Com	− 18.02 ± 0.27	− 16.05 ± 0.21	0.272 ± 0.008	0.308	NA	NA	NA
χ Dra	+43.70	+31.90 ± 0.14	0.175 ± 0.002	0.152–0.161	/	211 ± 56	0.198
h Dra	− 32.95 ± 0.03	− 21.00 ± 0.80	0.251 ± 0.036	0.195–0.219	\	71 ± 13	0.257
36 UMa	+8.71 ± 0.01	+8.69 ± 0.09	0.193 ± 0.011	0.173	/	107 ± 14	0.120
17 Crt	+5.85 ± 0.01	+5.80 ± 0.40	0.157 ± 0.013	0.158–0.167	|	12 ± 18	0.069
γ CrA B	− 50.40 ± 0.10	− 51.60 ± 0.30	0.139 ± 0.015	0.165	|	8 ± 80	0.080
ω Dra B	+28.42 ± 0.89	− 13.98 ± 0.02	0.307 ± 0.008	0.174–0.191	/	102 ± 16	0.134
θ Dra	+11.99 ± 0.70	− 8.23 ± 0.20	0.206 ± 0.004	0.164	NA	NA	NA
β Vir	+4.60 ± 0.01	+4.71 ± 0.08	0.162 ± 0.002	0.138–0.186	/	114 ± 3	0.077
F-star marginal detections							
τ PsA	− 16.11 ± 0.01	− 16.23 ± 0.09	0.156 ± 0.011	0.144–0.173	|	12 ± 75	0.047
γ Ser	+6.82 ± 0.03	+6.78 ± 0.09	0.153 ± 0.001	0.131–0.193	\	356 ± 14	0.075
F-star non-detections							
α Hyi	+20.31 ± 0.12	+8.70 ± 3.10	NA	NA	∗	∗	–
h UMa	−2.54	− 10.40 ± 0.70	0.240	NA	∗	∗	–
γ Cap	−33.75	− 31.20 ± 0.50	0.171	NA	/	107	–
δ Ser A	− 40.95 ± 0.21	− 41.50 ± 2.70	0.186 ± 0.001	NA	∗	∗	–
α Crv	+3.21 ± 0.02	+2.80 ± 0.30	0.279 ± 0.001	0.170–0.231	NA	NA	–
β TrA	+0.72 ± 0.08	+0.40 ± 0.60	NA	NA	∗	∗	–
δ Aql	− 31.70 ± 0.15	− 34.00 ± 0.20	0.241 ± 0.001	0.155–0.234	∗	∗	–
ω Dra A	− 47.74 ± 0.71	− 13.98 ± 0.02	0.240 ± 0.007	0.174–0.191	/	178 ± 16	–
δ Cap	− 21.73 ± 4.55	− 3.40 ± 0.80	0.298 ± 0.001	NA	∗	∗	–
υ UMa	+32.49 ± 0.58	+27.30 ± 4.10	0.210 ± 0.002	0.135	∗	∗	–
δ Gem	+3.37 ± 0.12	+4.10 ± 7.40	0.272 ± 0.001	0.174–0.182	∗	∗	–
τ Cyg	− 21.73 ± 0.03	− 20.90 ± 0.80	0.253 ± 0.001	0.176–0.243	NA	NA	–
η Lep	−1.33	− 2.14 ± 0.17	0.245	[1]0.141–0.184	\	83	–
ι Leo	− 10.62 ± 0.01	− 11.80 ± 0.20	0.230 ± 0.001	0.231–0.270	/	190 ± 21	–
10 UMa	+27.68 ± 0.04	+27.80 ± 2.80	0.216 ± 0.007	0.206–0.233	NA	NA	–
ψ Vel	+3.24 ± 0.01	+8.80 ± 1.80	0.365 ± 0.002	0.277	NA	NA	–
γ Cet	− 5.94 ± 1.33	− 4.90 ± 0.90	0.432 ± 0.002	NA	∗	∗	–
γ Tuc	− 2.31 ± 0.12	+18.40 ± 0.70	NA	NA	∗	∗	–
σ Cet	− 29.80 ± 0.01	− 27.50 ± 0.90	0.160 ± 0.001	0.157–0.197	|	0 ± 27	–
58 Oph	+10.34 ± 0.01	+10.20 ± 0.30	0.164 ± 0.018	0.197	|	8 ± 18	–
β Del	−28.36	− 33.90 ± 1.50	0.231	0.197–0.221	NA	NA	–
ψ Gem	+28.50 ± 0.12	+27.20 ± 0.70	0.217 ± 0.001	0.209–0.239	∗	∗	–
α CMi	− 5.36 ± 0.01	− 2.70 ± 1.01	0.165 ± 0.001	[1]0.137–0.174	/	201 ± 31	–
ι Peg	−26.66	− 5.50 ± 0.70	0.164 ± 0.003	0.150	/	131	–
ψ Peg	− 5.73 ± 0.01	− 5.37 ± 0.08	0.148 ± 0.001	0.121–0.176	/	71 ± 3	–
μ Cyg	+16.97 ± 0.02	+16.95 ± 0.16	0.178 ± 0.001	0.181	|	18 ± 14	–
α For	− 16.67 ± 0.05	− 17.14 ± 0.20	0.147 ± 0.054	0.162	/	127 ± 13	–
γ Lep	− 8.83 ± 0.01	− 9.29 ± 0.15	0.168 ± 0.001	0.143–0.183	\	441 ± 7	–
θ UMa	+14.47 ± 0.02	14.40 ± 0.20	0.141 ± 0.001	0.148–0.204	/	113 ± 14	–
ι Psc	+5.77 ± 0.01	+5.95 ± 0.08	0.161 ± 0.001	0.149–0.170	/	71 ± 26	–
σ02 UMa	− 3.13 ± 0.01	− 2.98 ± 0.09	0.135 ± 0.014	0.138–0.171	|	30 ± 32	–
δ Equ	− 15.76 ± 0.05	− 15.85 ± 0.07	0.166 ± 0.016	0.160	NA	NA	–
γ Del	− 6.00 ± 0.01	− 7.70 ± 0.30	0.110 ± 0.001	0.194	|	0 ± 18	–
6 Cet	+15.14 ± 0.01	+14.81 ± 0.09	0.174 ± 0.001	0.136–0.180	/	59 ± 23	–
ζ Cnc	− 5.24 ± 0.01	− 7.93 ± 0.08	0.143 ± 0.002	0.160–0.169	NA	NA	–
γ CrA A	− 52.82 ± 0.06	− 51.60 ± 0.30	0.128 ± 0.030	0.165	\	100 ± 45	–
HD 84117	+34.80 ± 0.01	+35.30 ± 0.44	0.151 ± 0.006	0.147–0.186	/	77 ± 41	–
η Cas	+8.68 ± 0.01	+8.44 ± 0.09	0.161 ± 0.001	0.138–0.172	/	38 ± 9	–
Definite detections, but uncertain which component							
κ Peg	− 21.45 ± 2.62	− 0.80 ± 0.20	0.237 ± 0.001	0.170	NA	NA	–
20 Oph	− 0.30 ± 0.01	− 1.60 ± 0.60	0.227 ± 0.001	NA	NA	NA	–

Notes. RV literature values from Anderson & Francis (2012) and [1]Buccino & Mauas (2008). Bisector velocity span based on points at 40 and 80 per cent *I*/*Ic*. Positive bisector slope with top leaning towards right is solar-type. ∗Bisectors are increasingly difficult to determine for stars with vsini > 20 km s^{-1} due to rotational broadening of spectral lines. NA = data not available. Bisectors not determined for unresolved spectroscopic binaries. α Crv not used for bisector analysis due to unusual line shape.

3.4.2 Stokes I asymmetry

Asymmetry in photospheric absorption lines provide information on the dynamics of gas flows in the stellar atmosphere (Dravins 1982), along the line of sight in the region where the lines are formed (Buonaura & Caccin 1982). The method of using bisectors to study stellar line asymmetry was pioneered by Gray (1981) and provides more information on conditions in the atmosphere than the alternative method of using a mirror image of an intensity line profile (Gray 1980). We calculated bisectors using the midpoint of horizontal lines connecting adjacent equal intensity points on the Stokes *I* profile as defined by Kulander & Jefferies (1966). Using a mean LSD profile to calculate the bisector was considered reasonable under the assumption that all spectral lines are affected in a similar way in the velocity field. The use of bisector analysis using Stokes *I* LSD profiles has been previously used for the G8 star ξ Bootis (Petit et al. 2005; Morgenthaler et al. 2012). An additional advantage of using mean bisectors is that it averages photometric noise in the data, and according to Gray (1982), it was not necessary to study intrinsic differences between lines for a first approximation study of bisectors. A limitation of using mean bisectors is that spectral lines of different depths can have different widths and shapes (Dravins 2008), which was also shown in a study of bisectors in A-Type stars by Landstreet et al. (2009) where a line shape difference was observed between weak and strong lines.

Two measures are used to characterize the Stokes *I* bisector; slope and velocity span. The slope of the bisector (Gray & Hatzes 1997) is the spectral line velocity at a point near the top, minus a point at the bottom, with a positive slope having the part of the line closest to the continuum leaning redwards. The exact depth of intensity points used in the measurement of bisector slope is not critical, but should be far enough from continuum and core to avoid measurement errors (Gray 1983). It is usually sufficient to estimate the slope visually from a bisector plot, while being careful to discount spurious points which are occasionally present. The second measurement of asymmetry, the velocity span, defined by Toner & Gray (1988) as the difference in velocity between two bisector points, which we take as $I/I_c = 0.8$ and 0.4 measured from the core to the continuum, similar to Hatzes et al. (2003). The bisector velocity span is considered a measure of the strength of convection in cool stars (Gray 1992), and is a useful measurement in stars where rotational broadening has not introduced errors due to a shallow line profile (Gray 1983). The bisector errors are determined by taking the standard deviation of bisector measurements from individual spectra. The Stokes *I* bisector slope and velocity span for our stars are shown in Table 5.

*3.4.3 **Stokes V amplitude***

The Stokes *V* profile contains important information on the stellar magnetic field (Grossmann-Doerth, Schussler & Solanki 1989), with the amplitudes of Stokes *V* signal providing information on the magnetic flux (Stenflo 1985). For unresolved weak solar magnetic fields (Solanki 1993), and stellar fields (Stenflo 1989), the amplitude of the Stokes *V* signal is proportional to B_l. We measured the amplitude (V/Ic) by taking the maximum height of the Stokes *V* signal above or below the continuum line. The Stokes *V* amplitudes of our stars are shown in Table 5.

3.5 Chromospheric emission (S-index)

Various methods have been used by researchers as indicators of stellar magnetism including, photometric variability (Hall 1991), asteroseismology (García et al. 2010), interferometry (Roettenbacher et al. 2016; Kochukhov et al. 2017), and non-thermal emission from chromospheric line cores including Ca II H&K (Wilson 1978; Duncan et al. 1991; Baliunas et al. 1995), Mg II (Howard & Stenflo 1972), Hα (Cincunegui, Díaz & Mauas 2007), and Ca II infrared triplet (Dempsey et al. 1993). The most widely used indirect indicator of stellar activity is the S-index introduced by Vaughan, Preston & Wilson (1978) as part of the decades long Mt Wilson survey of chromospheric activity in solar-type stars. The S-index is defined as,

$$S-\text{index} = \frac{aF_H + bF_K}{cF_{R_{HK}} + dF_{V_{HK}}} + e, \tag{2}$$

where F_H and F_K are the fluxes in the resonance lines from 20 Å-wide channels (with triangular profiles) centred at wavelengths, 396.8492 and 393.3682 nm, respectively (Duncan et al. 1991), compared to the flux at two bands in the continuum on the red and blue side of the H&K line. The coefficients determined for the ESPaDOnS and NARVAL spectropolarimeters (a,b,c,d,e) are taken from Marsden et al. (2014). The S-index is not calculated for 3 HARPSpol stars (α Hyi, β TrA, γ Tuc) with no coefficients available for use. We determined the S-index for our stars by calculating the mean and standard deviation from the individual spectra.

4 RESULTS

4.1 Stellar parameters

Table 1 lists the parameters for our 55 stars obtained from literature sources. The parameters which are significantly affected from a blend of binary components are identified in the table.

4.2 Magnetic detections

The rates of surface magnetic field detection for 51 of our stars are shown in Fig. 1. The figure does not include κ Peg and 20 Oph because we cannot determine if the detection comes from the F-star component. β CrB and δ Cap are not included because they could not be assigned a spectral type. The overall detection rate for our F-stars was 27 per cent (14 of 51). This detection rate is similar to that found in Marsden et al. (2014) who found magnetic detection rate of 32 per cent (6 of 19) for a sample of stars from F5-F9. A fossil field is present in β CrB, which shows a strong B_l of 735.8 $\pm$ 6.2 G. Magnetic fields are detected in every spectral type from F3V to F9V with a B_l ranging from 0.3 $\pm$ 0.1 G (36 UMa, F8V) to 8.3 $\pm$ 0.9 G (h Dra, F8V). We obtained no detections in F0 to F2 stars. ϵ Cet (F5V+F6V) and α Com (F5V+F6V) have definite detections which we assume comes from at least one of the F-star components. κ Peg and 20 Oph have definite detections, but we are not able to determine if the detection comes from the F-star component.

4.3 $|B_l|$ versus effective temperature ($T_{\rm eff}$)

Fig. 2 shows a plot of $|B_l|$ versus $T_{\rm eff}$ for all our 55 stars. The lack of magnetic detection for stars hotter than $T_{\rm eff} = 6720$ K (σ Boo, F3V)

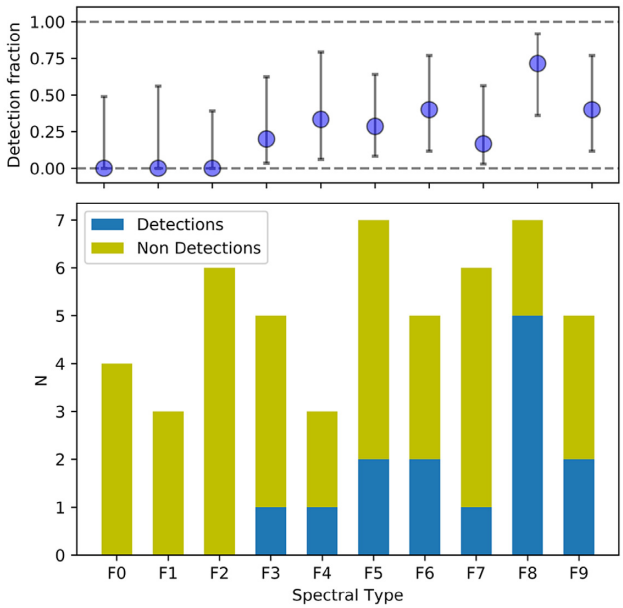

Figure 1. Histogram of detections/non-detections of surface magnetic fields for 51 of our stars from spectral type F0-F9. The detections include both marginal and definite detections. κ Peg and 20 Oph are omitted because we cannot determine if the detection came from the F-star component. β CrB and δ Cap are omitted because they are not assigned a spectral type. Overall detection rate is 27 per cent (14/51) and a 95 per cent confidence interval of 17–41 per cent. The upper panel shows the detection fraction along with 2σ error bars calculated using the original Wilson interval (Wilson 1927).

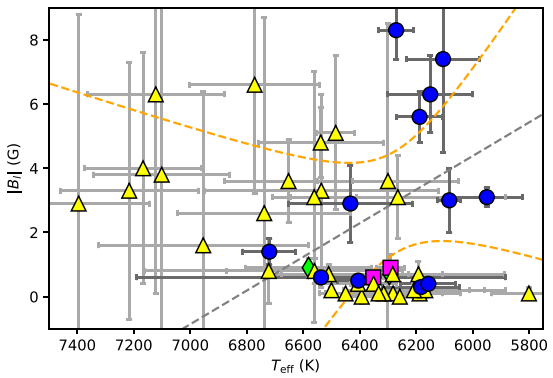

Figure 2. $|B_l|$ versus $T_{\rm eff}$ for 50 of our stars (excluding β CrB with a fossil field, and excluding 4 non-detections, α Hyi, α Crv, η Lep, and γ Cet, with large B_l and large uncertainties). The blue circles indicate definite magnetic detection on an F-star, yellow triangle indicates no detection, a magenta square is a marginal detection, while a green diamond is a definite detection but uncertain if detection is from the F-star or a companion. The dashed grey trend line and orange 95 per cent confidence intervals are shown for our 14 stars with magnetic detection, excluding β CrB. No significant trend observed between $T_{\rm eff}$ versus $|B_l|$.

is obvious. The only exception is β CrB ($T_{\rm eff}$ = 7980 K), shown in Fig. B1 with a fossil magnetic field. We find no significant trend between $|B_l|$ and $T_{\rm eff}$ for 14 stars with magnetic detections from F3 to F9 (Fig. 2). F-stars undergo a rapid increase in the depth of the outer convection zone when moving towards later spectral types, where $T_{\rm eff}$ can be considered a useful proxy for the convection zone depth (Pinsonneault, DePoy & Coffee 2001). In σ Boo, we find a definite magnetic field in a convection zone which is estimated

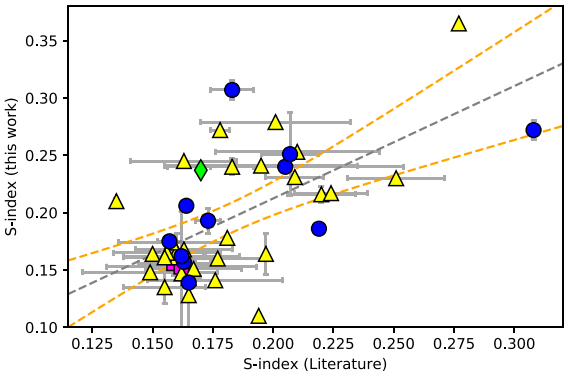

Figure 3. Chromospheric emission (S-index) found in this work versus the range of S-index from Pace (2013) and Buccino & Mauas (2008). The graph includes 44 stars which have both our S-index calculation and literature values. The dashed grey trend line and orange 95 per cent confidence intervals are shown. The error bars on the x-axis represent the range of values from the literature. The error bars on the y-axis represent the standard deviation for our determination. The symbols are the same as Fig. 2.

to be as thin as a few per cent of the stellar radius (Gilman 1980; Kuker & Rudiger 2007). The median $|B_l|$ of our 14 F-stars with a magnetic detection (excluding β CrB with a fossil field) is 2.2 G (mean 3.0 $\pm$ 2.7 G), which is similar to the mean of 3.3 G found in Marsden et al. (2014). While there is no linear increase in B_l strength with decreasing $T_{\rm eff}$, our results indicate the three hottest stars with detections (excluding β CrB) have among the weakest B_l. For stars cooler than $T_{\rm eff}$ 6400 K with magnetic detections there is no clear trend between $|B_l|$ and $T_{\rm eff}$.

4.4 Chromospheric emission (S-index)

The chromospheric emission (S-index) of our F-stars compared to the literature value of Pace (2013) and Buccino & Mauas (2008) are shown in Fig. 3. There is a correlation between our S-index values and the mid point of the range from Pace (2013), however the scatter for our F-stars, compared to literature values, is larger than Marsden et al. (2014, Fig. 4). In F-stars, as well as later spectral types, chromospheric emission is known to vary over time (Baliunas et al. 1995; Wright et al. 2004; Saikia et al. 2018), while our measurements are snapshots at a specific time. We cannot determine stellar magnetic activity cycles from our data, but can provide an indication of the strength of chromospheric emission compared to literature values, and see if this relates to a high or low point of a possible magnetic cycle. One explanation for the lack of magnetic detection of some of our stars is that we obtained spectra during low periods of the magnetic activity cycle. For 10 of 28 (36 per cent) of our stars with a non-magnetic detection, we measured the star at what is possibly a low point of the S-index range when comparing to literature values, therefore providing one possible explanation for the lack of magnetic detections.

Theoretical calculations using mixing-length theory indicate dynamo periods are short for F-stars, and increase towards later spectral types (Belvedere, Paterno & Stix 1980; Stix 1982). For an F5 star, the model by Belvedere et al. (1980) predicts a dynamo period of 0.88 yr, increasing by an order of magnitude to 9.5 yr for a G5 star. Olspert et al. (2017) estimated magnetic cycles for 10 F-type stars using a probabilistic analysis of Mt Wilson CaII H&K data, and determined cycle lengths ranging from 3.6 to 16.6 yr. The potentially short dynamo periods make early F-stars good targets for studies

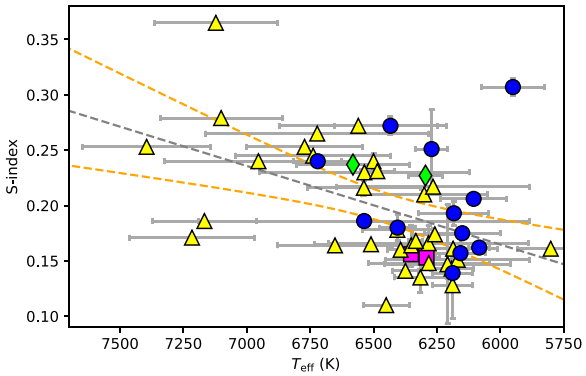

Figure 4. S-index versus $T_{\rm eff}$ for our 50 stars (excludes γ Cet which is a blend of F4V+A2Vn components and has a large S-index of 0.432). Three HARPSpol stars with no S-index calculation are excluded. β CrB with a fossil field is not included. The dashed grey trend line and orange 95 per cent confidence intervals shown. The symbols are the same as Fig. 2.

on stellar activity cycles, because the time required to measure a magnetic cycle may be as short as a few months, compared to years for later-type stars. See Mengel et al. (2016) for evidence for a very rapid ∼120 d magnetic cycle in τ Boo, an F7V star.

4.5 S-index versus $T_{\rm eff}$

Our plot of S-index versus $T_{\rm eff}$ (Fig. 4) shows an increase in S-index with increasing $T_{\rm eff}$ which is consistent with that found for F6 and later stars in Strassmeier et al. (1990). This contrasts with the lack of trend seen in our plot of $|B_l|$ versus $T_{\rm eff}$ (Fig. 2). While both S-index and B_l are indicators of stellar magnetic fields, they measure different parts of the stellar atmosphere and are not directly comparable. B_l is a measure of the large-scale photospheric magnetic field, and the S-index is a measure of chromospheric emission, caused by magnetic activity. The S-index is influenced by small scale magnetic fields which do not suffer from cancellation effects like B_l.

The S-index may also measure a basal chromospheric component unrelated to magnetic activity (Schrijver, Dobson & Radick 1989) which is caused by acoustic heating (Schrijver 1987; Ulmschneider, Priest & Rosner 1991). The S-index depends on both photospheric and chromospheric radiation, with photospheric line strength changing as a function of spectral type due to flux in the continuum windows (Cincunegui et al. 2007). Hotter stars have weaker photospheric absorption lines which leads to a larger S-index. S-index is a poor indicator of chromospheric activity in F-stars (Wolff, Heasley & Varsik 1985) due to the weakness in chromospheric emission and low contrast relative to the photospheric flux (Baliunas et al. 1995). The correlation between S-index and $T_{\rm eff}$ in our F-stars is possibly due to the changing strength of photospheric absorption lines rather than magnetic activity or basal chromospheric component.

It is interesting that γ Cet (F4V+A2Vn) has a very high S-index of 0.432 ± 0.24. Neither of the components from the blended spectra would be expected to create such a high S-index. The A2 component of γ Cet may be showing a high level of acoustic heating of the outer atmosphere, which is consistent with acoustic flux peaking in A-type stars (Walter, Matthews & Linsky 1995). Alternatively, A-type stars may have a different shape and strength to their Ca H&K lines, and potentially some Balmer lines blending into the continuum bands of the S-index. Therefore, the high S-index in γ Cet may not be due to chromospheric emission.

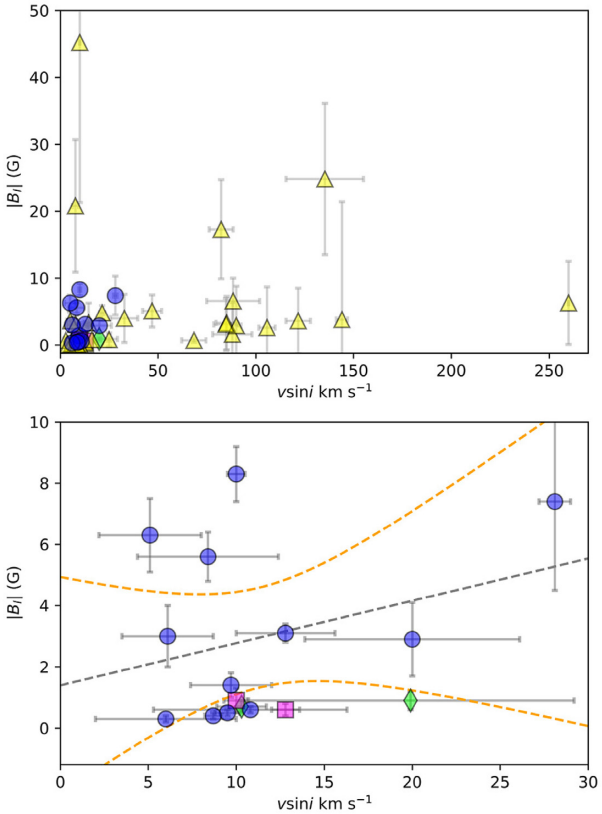

Figure 5. Top Figure. $|B_l|$ versus $v\sin i$ for 54 of our stars (excluding β CrB with a fossil field). Bottom figure. $v\sin i$ versus $|B_l|$ for 14 of our stars with a magnetic detection except β CrB. The dashed grey trend line and orange 95 per cent confidence intervals shown. No significant trend observed. The symbols are the same as Fig. 2.

4.6 $|B_l|$ versus stellar rotation

Stellar rotation is one of the major dynamo ingredients (Roberts & Soward 1992; Charbonneau & Steiner 2012) and the strength of the dynamo depends on the rate a star rotates (Noyes 1984; Simon & Fekel Jr 1987) along with other parameters such as differential rotation (Bullard & Gellman 1954; Spruit 2002) and the strength of convection (Parker 1955; Childress & Soward 1972). A plot of $|B_l|$ versus $v\sin i$ for our F-stars is shown in Fig. 5. We found no significant trend between $|B_l|$ and $v\sin i$ which differs from the positive correlation found for F-stars in Marsden et al. (2014, Fig. 13).

4.7 $|B_l|$ versus stellar age

The stars in our sample show a range of ages from 0.2 ± 0.6 to 5.2 ± 0.6 Gyr (Table 1). Our results in Fig. 6 show no correlation between $|B_l|$ and stellar age, which is different to the expected trend of a decrease in magnetic activity with increasing age shown in G,K,M stars by Saar (1991). When plotted into bins of 1.0 Gyr (Fig. 7) we find the highest rate of magnetic detection is in stars aged 2–3 Gyr (with the exception of the single 5.2 Gyr star), which is broadly comparable to that found in Marsden et al. (2014, Fig. 6).

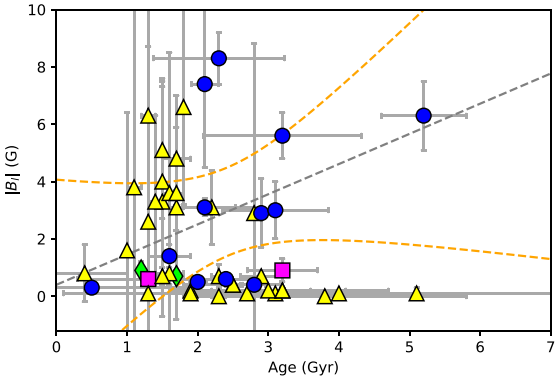

Figure 6. $|B_l|$ versus stellar age for 50 of our stars, excluding β CrB (fossil field) and excluding 4 stars (α Hyi, β TrA, θ UMa, and γ Cet) with no detection and large B_l with large uncertainties. The dashed grey trend line and orange 95 per cent confidence intervals shown for our 14 stars with a magnetic detection excluding β CrB. No significant trend observed. The symbols are the same as Fig. 2.

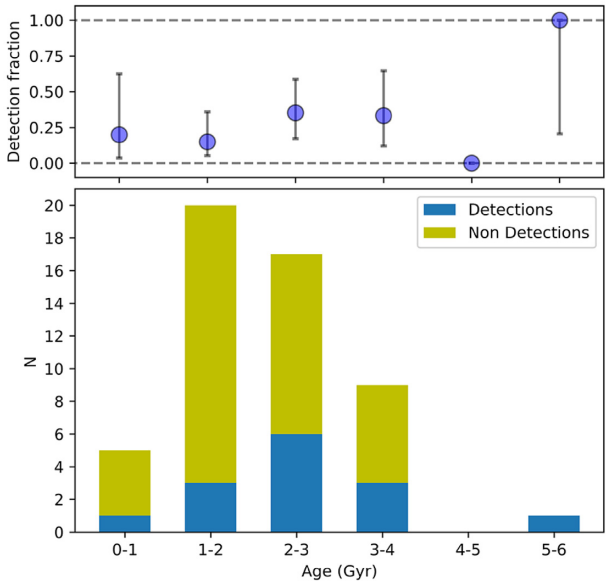

Figure 7. Histogram magnetic detection rate versus age for our 52 F-stars grouped into 1.0 Gyr bins. The detections include both definite and marginal detections. κ Peg and 20 Oph were omitted because we cannot determine if the detection came from the F-star component. β CrB with a fossil field was omitted. The upper panel shows the detection fraction along with 2σ error bars calculated using the original Wilson interval (Wilson 1927).

4.8 Bisector span versus $T_{\rm eff}$

Stokes *I* bisector velocity span (proxy for strength of convection) for our F-stars ranges from 0 to 441 m s^{-1} (Table 5). Our bisector velocity span for α CMi was 201 m s^{-1} compares with a value of 500 m s^{-1} in Gray (2010). Our results are consistent with the higher velocity spans found in F-stars compared to later spectral types (Gray 2010). Similarly, Kuker & Rudiger (2005, 2007) found F-type stars have higher convection velocities and shorter convective turnover times compared to solar-type stars, with an order of magnitude increase in convection velocity for a 1.4 $M_\odot$ star compared to the Sun. We do not find an increase in bisector

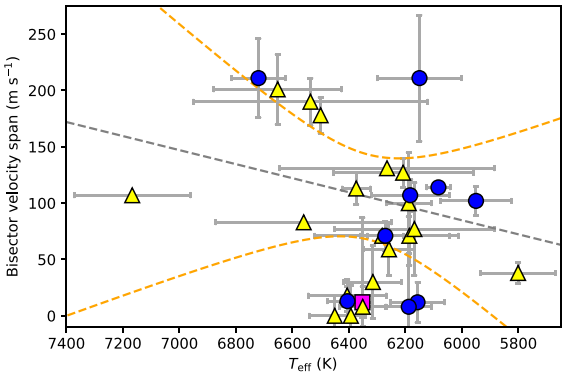

Figure 8. Bisector velocity span versus $T_{\rm eff}$ for our 31 stars with a calculated bisector span. β CrB with a fossil field is not included. The dashed grey trend line and orange 95 per cent confidence intervals shown. No significant trend observed. The symbols are the same as Fig. 2.

velocity span with increasing $T_{\rm eff}$ across the range of stars from F9 to F0 (Fig. 8).

We find that 7 of 12 (58 per cent) of our stars with a magnetic detection have a bisector span $\geq$ 100 m s^{-1}, compared to 7 of 20 (35 per cent) of stars without a magnetic detection with measured bisectors. This result is consistent with the expectation that stars with stronger convection are more likely to show a magnetic field. An analysis of the slope of the Stokes *I* bisector (Table 5) shows 53 per cent (17 of 32) of stellar components have solar-type bisectors (positive slope), 25 per cent (8 of 32) have no slope (velocity span not significantly different from zero), and 22 per cent (7 of 32) have reversed bisectors. We do not see a trend of reversing bisectors towards the hotter stars. The phenomenon of reversed bisectors (Gray & Toner 1986; Gray 1989; Gray & Nagel 1989) has been associated with the granulation boundary (Gray 1982) a location on the HR-diagram where a lack of outer convection zone results in a net upward velocities in the stellar atmosphere.

4.9 $v\sin i$ versus $T_{\rm eff}$

Due to rotational braking (Schatzman 1962; Weber & Davis Jr 1967; Skumanich 1972) which is known to occur around mid F-stars (Kraft 1967), we expect to see a large decrease in $v\sin i$ with decreasing $T_{\rm eff}$ corresponding to the onset of dynamo magnetic fields. Our plot in Fig. 9 shows a large decrease in $v\sin i$ occurring at $T_{\rm eff} \approx 6400$ K, which is consistent with an onset of dynamo magnetic fields which causes magnetic braking. All our stars with magnetic detections appear to have spun down, which is consistent with expectations due to rotational breaking. Fig. 9 also shows the strength of $|B_l|$ does not appear to correlate with either $T_{\rm eff}$ (see Section 4.3) or $v\sin i$.

4.10 SNR versus $T_{\rm eff}$

In Fig. 10 we plot SNR versus $T_{\rm eff}$ (Stokes *V* LSD) for all our 55 stars to see if there is a difference between the early and late F-stars which may explain the lack of magnetic detections in F0-F2 stars. The SNR is taken from values listed in Table 4. The mean SNR for our F0-F2 stars is 41515 $\pm$ 30085 compared to F3-F9 stars 84394 $\pm$ 42229. The lower SNR in the F0-F2 stars made it more difficult to detect the expected weak dynamo fields if they were present, however we detected magnetic fields in four later F-stars

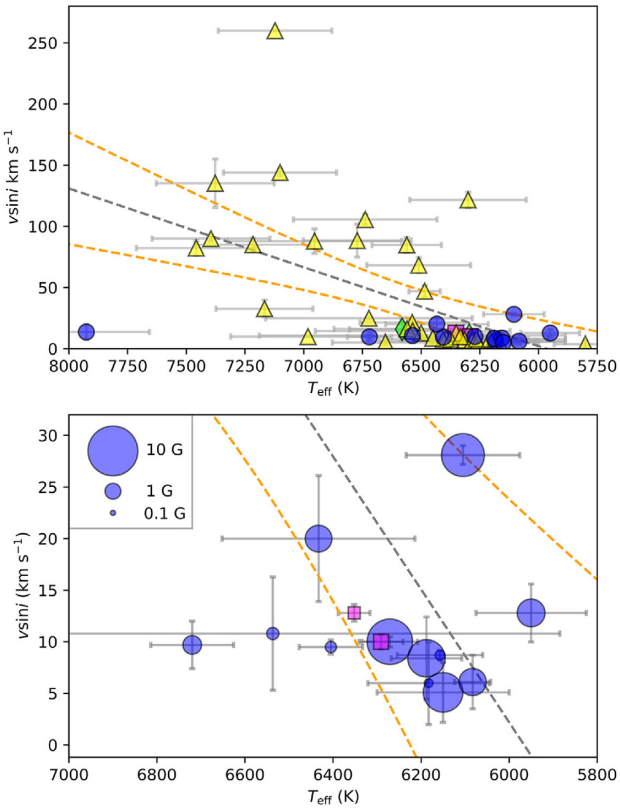

Figure 9. Figure at top shows $v \sin i$ versus $T_{\rm eff}$ for all our 55 stars. The dashed grey trend line and orange 95 per cent confidence intervals shown. The symbols are the same as Fig. 2. The bottom figure shows the expanded region comprising 14 stars with a magnetic detection, except β CrB. Circle radius and square width is proportional to B_l.

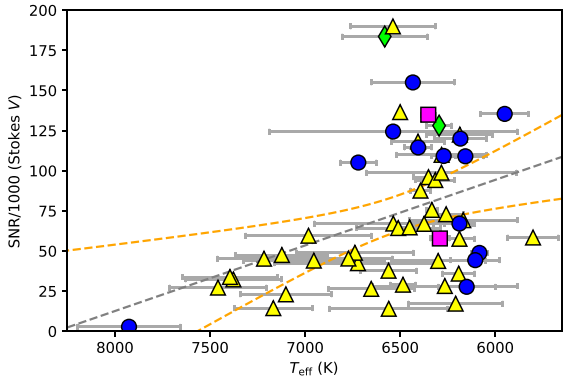

Figure 10. SNR (LSD Stokes V) versus $T_{\rm eff}$ for all our 55 stars. The dashed grey trend line and orange 95 per cent confidence intervals shown. The smbols are the same as Fig. 2.

from the BRITEpol sample with SNR comparable to the F0-F2 stars.

4.11 Stokes V amplitude versus $|B_l|$

In Fig. 11 we plot the Stokes V amplitude versus $|B_l|$ for 11 stars with a magnetic detection, excluding 3 stars which are unresolved spectroscopic binaries, and β CrB with a fossil field. We found a significant positive correlation for our 11 F-stars, which is in

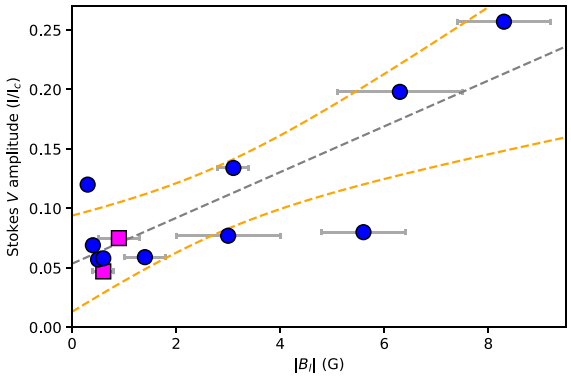

Figure 11. LSD Stokes V amplitude versus $|B_l|$ for 11 stars with a magnetic detection. Excluded is β CrB with a fossil field and 3 unresolved spectroscopic binaries. The dashed grey trend line and orange 95 per cent confidence intervals shown. Significant trend observed. The symbols are the same as Fig. 2.

agreement with the trend discussed by Stenflo (1989) where an increase in B_l results in a larger Stokes V amplitude.

5 DISCUSSION

Early F-type stars have superficial outer convection zones which at some effective temperature become too thin to sustain a magnetic dynamo. Our snapshot survey includes 53 F-type stars from spectral types F0-F9 plus 2 chemically peculiar stars β CrB and δ Cap. Our sample covers 27 per cent of the F-stars brighter than magnitude 5 listed in the Bright Star Catalogue (Table 2). The number of stars in our survey allows a study of the high temperature boundary for dynamo magnetic fields with an expected detection rate similar to Marsden et al. (2014) who found photospheric magnetic fields in 32 per cent of F-stars (6 of 19). We found a similar result with magnetic fields detected in 27 per cent (14 of 51) of our F-stars. Since fossil fields have an incidence of only about 10 per cent in higher mass stars and fall to about 1 per cent in stars with lower masses (Sikora et al. 2018) we would need a larger sample of early F-stars to explore more fully the low temperature boundary for fossil fields.

The hottest star in our sample β CrB is a well known chemically peculiar star with a fossil field and many published magnetic curves (Preston & Sturch 1967; Wolff & Wolff 1970; Borra & Landstreet 1980; Kurtz 1989; Han et al. 2018). The magnetic curve of β CrB has been modelled to represent a superposition of a dipole and a quadrupole field (Bagnulo et al. 2000) and shows a sinusoidal shape (Han et al. 2018) with a maximum $|B_l|$ of 653 G (Borra & Landstreet 1980), 754 G (Borra, Fletcher & Poeckert 1981), and 762 G (Wade et al. 2000). Our maximum measured $|B_l|$ of 735.8 $\pm$ 6.2 G is consistent with these published measurements.

Fossil magnetic fields have been detected in stars as cool as 6400 K. See for example HD 213637, $T_{\rm eff}$ = 6400 K (Kochukhov 2003), HD 101065, $T_{\rm eff}$ = 6400 K (Shulyak, Ryabchikova & Kochukhov 2013), ρ Pup $T_{\rm eff}$ = 6500–6850 K (Neiner, Wade & Sikora 2017b), HD 24712, $T_{\rm eff}$ = 7250 K (Shulyak et al. 2013), HD 188774 $T_{\rm eff}$ = 7600 K (Neiner & Lampens 2015), and HD 115226, $T_{\rm eff}$ = 7640 K (Kochukhov et al. 2008). These low temperature fossil fields may have large B_l, similar to β CrB, or weak B_l as shown by recently discovered Ap and Fp stars with sub-Gauss magnetic fields. Ultra-weak fossil fields were first detected in Vega (A0V) by Lignières et al. (2009) with B_l strength of 0.6 $\pm$ 0.3 G (Stokes

V SNR of 1500 per 1.8 km s^{-1}) and have been detected in stars as cool as F2 (Neiner et al. 2017b).

We detect photospheric magnetic fields in all spectral classes from F3V-F9V (Figs B2–B15), and no evidence of magnetic fields in 13 stars with spectral types F0 to F2. The hottest F-star with a definite magnetic detection is σ Boo (F3V), with an outer convection zone thickness less than few per cent of the stellar radius. The $|B_l|$ strengths for stars from F3-F9 ranges from 0.3 $\pm$ 0.1 G to 8.3 $\pm$ 0.9 G (median 2.2 G). χ Dra (F7V) is an interesting star which shows a relatively stable Stokes V magnetic signature with some characteristics of a fossil field. These multiple observations are not included here, but are being presented in a future paper using Zeeman Doppler imaging to map the magnetic field of χ Dra (Seach et al. in preparation).

From our magnetic snapshot survey with most stars having observations from only a single night, it is not possible to say definitely whether magnetic fields in our F-stars are dynamo or weak fossil fields. With $|B_l|$ ranging from 0.3 to 8.0 G, and sub-Gauss fossil fields existing in stars as cool as F2, the strength of magnetic field cannot be used solely to distinguish between fossil and dynamo fields. Another possible distinction with fossil fields having simple and stable Stokes V signatures and dynamo fields having complex Stokes V signatures does not always apply. For example, the Stokes V signatures of our 14 F-stars with a magnetic detection (with the exception of α Com) are not much more complex than that of β CrB with a fossil field (Appendix B). Stars with fossil fields can also show complex Stokes V signatures similar to those expected in dynamo fields. Examples of complex Stokes V signatures in stars with a fossil field include γ Gem, an Am star with a weak fossil field (Blazère, Neiner & Petit 2016), and ρ Pup, a δ Scuti F2m star (Neiner et al. 2017b), and several fast rotating stars with fossil fields (Silvester et al. 2012).

A possible reason we did not detect magnetic fields in stars earlier than spectral type F3V is due to the lower sensitivity of the spectra obtained for the early F-stars. However, even though the SNR of our F0-F2 stars is mostly lower than the F3-F9 stars, it is still possible to detect magnetic fields in the early F-star sample. We detected four late F-stars with an SNR comparable to the F0-F2 sample (Fig. 10), therefore, the lower SNR of the F0-F2 spectra was unlikely to be the sole reason for lack of magnetic field detection in our early F-stars. Another possibility for a lack of magnetic field detection in our early F-stars is the presence of cancellation effects. B_l is an average of the line of sight component of the magnetic field vector over the visible hemisphere, therefore regions of opposite polarity may cancel out, resulting in a field too weak to detect. With the suggestion by Giampapa & Rosner (1984) that spots on early F-type stars are small and evenly distributed over the stellar surface, this may indicate there are small areas of opposite polarity which may cause cancellation effects to be more pronounced in early F-stars compared with late F-stars.

We find a positive correlation between $T_{\rm eff}$ and S-index (Fig. 4) from spectral types F0V-F9V. In cool stars from spectral types G and later, the S-index is an indicator of chromospheric emission related to areas of magnetic activity on the star's surface. The higher levels of chromospheric emission for our early F-stars may be an indication of a basal chromospheric component which is unrelated to magnetic activity. Therefore the S-index may not be a good indicator of magnetic activity in early F-stars (Schrijver et al. 1989). The S-index is also dependent on the spectral type of the star, and our results may indicate the well known temperature dependence on chromospheric activity (Middelkoop 1982; Noyes 1984). We find no correlation between $|B_l|$ and stellar age (Fig. 6). This is different from the trend expected where stellar activity declines with age as shown by Marsden et al. (2013) and studies on stellar activity proxies using on Mg II, Ca IV, Hα, and X-ray emission (Hartmann & Noyes 1987). We have shown for our F-stars there is a positive correlation between the Stokes V amplitude and $|B_l|$ which was consistent with expectations for stars with weak magnetic fields. We do not find a correlation between $|B_l|$ and $T_{\rm eff}$ or $v \sin i$. Magnetic mapping of the surface of early F-type stars with Zeeman Doppler imaging (Kochukhov 2016) will be valuable in providing further details about the nature of stellar magnetism.

6 CONCLUSIONS

We detect photospheric magnetic fields in 14 out of 51 F-stars from a survey of spectral types from F0V to F9V. There are 12 definite detections, 2 marginal detections, and 2 binary stars with a detection but we were unable to determine if it came from the F-star component. As expected, surface magnetic fields of many of our F-stars are weak, with 6 of 14 stars having $|B_l| < 1.0$ G. There is a positive correlation between Stokes V amplitude and $|B_l|$. We found no correlation between $|B_l|$ and $T_{\rm eff}$, $|B_l|$ and $v \sin i$, or $|B_l|$ and age. Further work on magnetic mapping of interesting targets from this work is planned in the future, in order to gain more insights into stellar magnetism in stars with shallow convection zones.

ACKNOWLEDGEMENTS

This research was based on observations obtained at the Canada-France-Hawaii Telescope (CFHT) which is operated by the National Research Council of Canada, the Institut National des Sciences de l'Univers of the Centre National de la Recherche Scientifique of France, and the University of Hawaii. This work is based on observations obtained at the Bernard Lyot Telescope (TBL, Pic du Midi, France) of the Midi-Pyrénées Observatory, which is operated by the Institut National des Sciences de l'Univers of the Centre National de la Recherche Scientifique of France. Observations were collected at the European Organisation for Astronomical Research in the Southern Hemisphere under ESO programmes 094.D–0274(A), 097.D–0156(A), 095.D–0155(B). This research was supported by an Australian Government Research Training Program (RTP) Scholarship. This research has made use of the SIMBAD data base, operated at CDS, Strasbourg, France. This research has made use of the VizieR catalogue access tool, CDS, Strasbourg, France. This work has made use of data from the European Space Agency (ESA) mission *Gaia* (https://www.cosmos.esa.int/gaia), processed by the *Gaia* Data Processing and Analysis Consortium (DPAC, https://www.cosmos.esa.int/web/gaia/dpac/consortium). Funding for the DPAC has been provided by national institutions, in particular the institutions participating in the *Gaia* Multilateral Agreement.

REFERENCES

Abramowitz M., Stegun A., 1964, Handbook of Mathematical Functions, 9th edn. Dover Publications, USA
Abt H. A., 2009, ApJS, 180, 117
Abt H., Levy S., 1976, ApJS, 30, 273
Adelman S. J., Bolcal C., Hill G., Koçer D., 1991, MNRAS, 252, 329
Aguilera-Gómez C., Ramírez I., Chanamé J., 2018, A&A, 614, A55
Anderson E., Francis C., 2012, Astron. Lett., 38, 331
Aurière M., 2003, EAS Pub. Ser., 9, 105
Babcock H., 1947, ApJ, 105, 105

Babcock H. W., 1960, ApJ, 132, 521
Bagnulo S., Landolfi M., Mathys G., Landi Degl'Innocenti M., 2000, A&A, 358, 929
Bagnulo S., Landstreet J., Fossati L., Kochukhov O., 2012, A&A, 538, A129
Baliunas S. et al., 1995, ApJ, 438, 269
Barlow D. J., Scarfe C. D., 1977, PASP, 89, 857
Baschek B., Reimers D., 1969, A&A, 2, 240
Behr B. B., Hajian A. R., Cenko A. T., Murison M., McMillan R. S., Hindsley R., Meade J., 2009, ApJ, 705, 543
Behr B. B., Cenko A. T., Hajian A. R., McMillan R. S., Murison M., Meade J., Hindsley R., 2011, AJ, 142, 6
Belvedere G., Paterno L., Stix M., 1980, A&A, 91, 328
Beskin V., Balogh A., Falanga M., Lyutikov M., Mereghetti S., Piran T., Treumann R., eds, 2016, The Strongest Magnetic Fields in the Universe. Springer-Verlag, New York, p. 583
Blazère A., Neiner C., Petit P., 2016, MNRAS, 459, L81
Böhm-Vitense E., Dettmann T., 1980, ApJ, 236, 560
Borra E., Landstreet J., 1980, ApJS, 42, 421
Borra E. F., Fletcher J., Poeckert R., 1981, ApJ, 247, 569
Braithwaite J., Spruit H. C., 2017, Royal Soc. Open Sci., 4, 160271
Brandenburg A., Subramanian K., 2005, Phys. Rep., 417, 1
Buccino A. P., Mauas P. J., 2008, A&A, 483, 903
Bullard E., Gellman H., 1954, Philos. Trans. Royal Soc. A, 247, 213
Buonaura B., Caccin B., 1982, A&A, 111, 113
Cakirli O., İbanoğlu C., Frasca A., 2007, A&A, 474, 579
Campbell W., 1899, ApJ, 10, 178
Casagrande L., Schoenrich R., Asplund M., Cassisi S., Ramirez I., Melendez J., Bensby T., Feltzing S., 2011, A&A, 530, A138
Castelaz M. W., 1989, AJ, 97, 1184
Chang S.-W., Protopapas P., Kim D.-W., Byun Y.-I., 2013, AJ, 145, 132
Charbonneau P., Steiner O., 2012, Solar and Stellar Dynamos. Springer, Berlin, Heidelberg
Chen P., Liu J., Shan H., 2017, AJ, 153, 218
Childress S., Soward A., 1972, Phys. Rev. Lett., 29, 837
Cincunegui C., Díaz R., Mauas P., 2007, A&A, 469, 309
Conti P. S., 1970, PASP, 83, 207
Cotten T. H., Song I., 2016, ApJS, 225, 15
Cousins A. W. J., 1971, R. Obs. Ann., 7, 86
Cowling T., 1945, MNRAS, 105, 166
David T. J., Hillenbrand L. A., 2015, ApJ, 804, 146
Da Silva R., de Mello G. P., Milone A., da Silva L., Ribeiro L., Rocha-Pinto H., 2012, A&A, 542, A84
Demarque P., Roeder R., 1967, ApJ, 147, 1188
Dempsey R. C., Bopp B. W., Henry G. W., Hall D. S., 1993, ApJS, 86, 293
Docobo J., Andrade M., 2013, MNRAS, 428, 321
Dolag K., Kachelriess M., Ostapchenko S., Tomas R., 2010, ApJ, 727, L4
Donati J.-F., 2003, in Javier T.-B., Jorge S. A., eds, ASP Conf. Ser. Vol. 307, Solar Polarization. Astron Soc. Pac., San Francisco, p. 41
Donati J.-F., Semel M., Rees D., 1992, A&A, 265, 669
Donati J.-F., Semel M., Carter B., Rees D., Cameron A. C., 1997, MNRAS, 291, 658
Donati J.-F., Catala C., Landstreet J., Petit P., 2006a, in Casini R., Lites B. W., eds, ASP Conf. Ser., Vol. 358, Solar Polarization 4. Astron. Soc. Pac., San Francisco, p. 362
Donati J.-F. et al., 2006b, MNRAS, 370, 629
Dravins D., 1982, ARA&A, 20, 61
Dravins D., 2008, A&A, 492, 199
Duncan D. K. et al., 1991, ApJS, 76, 383
Duquennoy A., Mayor M., 1988, A&A, 195, 129
Duquennoy A., Mayor M., Halbwachs J.-L., 1991, ApJS, 88, 281
Edwards T., 1976, AJ, 81, 245
Eggen O. J., 1960, MNRAS, 120, 540
Eggleton P., Pringle J., Division N. A. T. O. S. A., 1985, Interacting Binaries. D. Reidel Pub. Co., Dordrecht
Ertel S. et al., 2016, A&A, 595, A44
Evans D. S., Menzies A., Stoy R., 1957, MNRAS, 117, 534
Fekel F. C., Tomkin J., Williamson M. H., 2009, AJ, 137, 3900
Finsen W., 1955, MNASSA, 14, 84
Fracassini L. P., Pastori L., Covino S., Pozzi A., 2001, A&A, 367, 521
Fuhrmann K., 2008, MNRAS, 384, 173
Gaia collaboration et al., 2018, A&A, 616, A1
García R. A., Mathur S., Salabert D., Ballot J., Régulo C., Metcalfe T. S., Baglin A., 2010, Science, 329, 1032
Gasteyer C., 1954, AJ, 59, 243
Giampapa M. S., Rosner R., 1984, ApJ, 286, L19
Gilman P. A., 1980, IAU Colloquium, Vol 51. Cambridge Univ. Press, Cambridge, p. 19
Glass I. S., 1974, MNSSA, 33, 53
Glebocki R., Gnacinski P., 2005, 13th Cambridge Workshop on Cool Stars, Stellar Systems and the Sun, Vol. 560. Hamburg, Germany, p. 571
Gomez A., Abt H. A., 1982, PASP, 94, 650
Gontcharov G., 2012, Astron. Lett, 38, 771
Gontcharov G. A., Kiyaeva O. V., 2010, New Astron., 15, 324
Gray D., 1980, ApJ, 235, 508
Gray D., 1981, ApJ, 251, 583
Gray D. F., 1982, ApJ, 255, 200
Gray D. F., 1983, PASP, 95, 252
Gray D. F., 1989, PASP, 101, 832
Gray D., 1992, in Page D., Hirsch J. G., eds, ASP Conf. Ser. Vol. 26, Cool Stars, Stellar Systems, and the Sun, Proceedings of the 7th Cambridge Workshop. Astron. Soc. Pac., San Francisco, p. 127
Gray D. F., 2010, ApJ, 710, 1003
Gray D. F., Hatzes A. P., 1997, ApJ, 490, 412
Gray D. F., Nagel T., 1989, ApJ, 341, 421
Gray D. F., Toner C. G., 1986, PASP, 98, 499
Gray R., Napier M., Winkler L., 2001, AJ, 121, 2148
Gray R. O., Corbally C. J., Garrison R. F., McFadden M. T., Bubar E. J., McGahee C. E., O'Donoghue A. A., Knox E. R., 2006, AJ, 132, 161
Griffin R., 1999, Observatory, 119, 272
Griffin R., 2000, Observatory, 120, 1
Grossmann-Doerth U., Schuessler M., Solanki S. K., 1989, A&A, 221, 338
Grunhut J. H. et al., 2017, MNRAS, 465, 2432
Gullikson K., Kraus A., Dodson-Robinson S., 2016, AJ, 152, 40
Hale G. E., 1908, ApJ, 28, 315
Hall D. S., 1991, in Tuominen I., Moss D., Rudiger G., eds, IAU Colloquium, Vol. 130. Cambridge Univ. Press, Cambridge, p. 353
Han I. et al., 2018, MNRAS, 479, 1427
Hartkopf W. I., McAlister H. A., Franz O. G., 1989, AJ, 98, 1014
Hartmann L. W., Noyes R. W., 1987, ARA&A, 25, 271
Hatzes A. P., Cochran W. D., Endl M., McArthur B., Paulson D. B., Walker G. A., Campbell B., Yang S., 2003, ApJ, 599, 1383
Heintz W., 1986, ApJS, 64, 1
Herald D., Sinnott R, 2014, JBAA, 124, 247
Hoffleit D., 1991, Catalogue of bright stars, 3rd edn. Yale University Observatory, New Haven, CT
Howard R., Stenflo J. O., 1972, Sol. Phys., 22, 402
Isaacson H., Fischer D., 2010, ApJ, 725, 875
Jofre P., Heiter U., Maia M., Soubiran C., Worley C., Hawkins K., Blanco-Cuaresma S., Rodrigo C., 2018, Res. Notes AAS, 2, 152
Johnson H., Morgan W., 1953, ApJ, 117, 313
Kochukhov O., 2003, A&A, 404, 669
Kochukhov O., 2016, in Rozelot J.-P., Neiner C., eds, Cartography of the Sun and the Stars. Springer, Berlin, p. 77.
Kochukhov O., Ryabchikova T., Bagnulo S., Curto G. L., 2008, A&A, 479, L29
Kochukhov O. et al., 2017, Astron. Nachr., 338, 428
Konacki M., Muterspaugh M. W., Kulkarni S. R., Hełminiak K. G., 2010, ApJ, 719, 1293
Kraft R. P., 1967, ApJ, 150, 551
Krause F., Radler K., 1980, Mean-Field Magnetohydrodynamics and Dynamo Theory. Akademie-Verlag, Berlin
Kuker M., Rudiger G., 2005, A&A, 433, 1023
Kuker M., Rudiger G., 2007, Astron. Nachr., 328, 1050
Kulander J. L., Jefferies J. T., 1966, ApJ, 146, 194
Kurtz D., 1989, MNRAS, 238, 261

Landstreet J., Kupka F., Ford H., Officer T., Sigut T., Silaj J., Strasser S., Townshend A., 2009, A&A, 503, 973
Lignières F., Petit P., Böhm T., Aurière M., 2009, A&A, 500, L41
Lindegren L., Dravins D., 2003, A&A, 401, 1185
Lipunov V. et al., 2016, A&A, 588, A90
Makaganiuk V. et al., 2011, A&A, 525, A97
Malkov O. Y., Tamazian V. S., Docobo J. A., Chulkov D. A., 2012, A&A, 546, A69
Marsakov V. A., Shevelev Y. G., 1995, Bull. Inf. Cent. Donnees Stellaires, 47, 13
Marsden S., Petit P., Jeffers S., do Nascimento J.-D., Carter B., Brown C., 2013, Proc. IAU Symp. 302, 9, 138
Marsden S. et al., 2014, MNRAS, 444, 3517
Martinez-Arnaiz R., Maldonado J., Montes D., Eiroa C., Montesinos B., 2010, A&A, 520, A79
Mason B. D., Wycoff G. L., Hartkopf W. I., Douglass G. G., Worley C. E., 2001, AJ, 122, 3466
Mathys G., 1995, A&A, 293, 733
McDonald I., Zijlstra A. A., Watson R. A., 2017, MNRAS, 471, 770
McLaughlin D. B., 1947, ApJ, 105, 497
Mengel M. et al., 2016, MNRAS, 459, 4325
Mestel L., 1966, MNRAS, 133, 265
Mestel L., 1967, in Cameron R., ed., Magnetic and Related Stars, Mono Book Corp., p. 101
Mestel L., 2012, International Series of Monographs on Physics, Vol. 154, Stellar Magnetism, 2nd edn. OUP, Oxford
Mestel L., Spitzer L., 1956, MNRAS, 116, 503
Middelkoop F., 1982, A&A, 107, 31
Mizusawa T. F., Rebull L. M., Stauffer J. R., Bryden G., Meyer M., Song I., 2012, AJ, 144, 135
Moffatt H., 1978, Magnetic Field Generation in Electrically Conducting Fluids. Cambridge Univ. Press, Cambridge
Montesinos B. et al., 2016, A&A, 593, A51
Morgenthaler A. et al., 2012, A&A, 540, A138
Moss D., 2001, in Mathys G., Solanki S. K., Wickramasinghe D. T., eds, ASP Conf. Ser. Vol. 248, Magnetic Fields Across the Hertzsprung-Russell Diagram. Astron. Soc. Pac., San Francisco, p. 305
Moutou C. et al., 2007, A&A, 473, 651
Muterspaugh M. W., Lane B. F., Konacki M., Burke B. F., Colavita M. M., Kulkarni S. R., Shao M., 2005, AJ, 130, 2866
Muterspaugh M. W. et al., 2008, AJ, 135, 766
Muterspaugh M. W., Lane B. F., Kulkarni S. R., Konacki M., Burke B. F., Colavita M. M., Shao M., 2010, AJ, 140, 1631
Muterspaugh M. W. et al., 2015, AJ, 150, 140
Neiner C., Lampens P., 2015, MNRAS, 454, L86
Neiner C., Mathis S., Alecian E., Emeriau C., Grunhut J., 2015, IAU Symposium, 305, 61
Neiner C., Wade G., Marsden S., Blazère A., 2017a, in Zwintz K., Poretti E., eds, Second BRITE-Constellation Science Conference, Vol. 5, Polish Astronomical Society, Innsbruck, Austria, p. 86
Neiner C., Wade G., Sikora J., 2017b, MNRAS, 468, L46
Noyes R. W., 1984, Adv. Space Res., 4, 151
O'Toole S., Jones H., Tinney C., Butler R., Marcy G., Carter B., Bailey J., Wittenmyer R., 2009, ApJ, 701, 1732
Olspert N., Lehtinen J. J., Käpylä M. J., Pelt J., Grigorievskiy A., 2018, A&A, 619, A6
Owens M. J., Forsyth R. J., 2013, Living Rev. Sol. Phys., 10, 5
Pace G., 2013, A&A, 551, L8
Parker E. N., 1955, ApJ, 122, 293
Parker E., 1979, Cosmical Magnetic Fields: Their Origin and Their Activity. Clarendon Press, Oxford
Petit P. et al., 2005, MNRAS, 361, 837
Pinsonneault M., DePoy D., Coffee M., 2001, ApJ, 556, L59
Piskunov N., Valenti J., 2002, A&A, 385, 1095
Piskunov N. et al., 2011, Messenger, 143, 7
Preston G. W., Sturch C., 1967, in Cameron R., ed., Magnetic and Related Stars, Mono Book Corp., p. 111
Prieto C.A., Lambert D. L., 1999, Astron. Astrophys., 352, 555
Raghavan D. et al., 2010, ApJS, 190, 1
Reiners A., Basri G., 2009, A&A, 496, 787
Rice J. B., Hill G. a., 1988, PASP, 100, 73
Roberts P. H., Soward A. M., 1992, Annu. Rev. Fluid Mech., 24, 459
Roettenbacher R. M. et al., 2016, Nature, 533, 217
Roman N. G., 1950, ApJ, 112, 554
Ryabchikova T., Piskunov N., Kurucz R., Stempels H., Heiter U., Pakhomov Y., Barklem P. S., 2015, Phys. Scr., 90, 054005
Saar S., 1991, in Tuominen I., Moss D., Rudiger G., eds, IAU Colloquium, Vol 130. Cambridge Univ. Press, Cambridge, p. 389
Saikia S. B. et al., 2018, A&A, 616, A108
Samus N., Kazarovets E., Durlevich O., Kireeva N., Pastukhova E., 2017, Astron. Rep., 61, 80
Sato S., Cuntz M., Olvera C. G., Jack D., Schr'oder K.-P., 2014, Int. J. Astrobiol., 13, 244
Scardia M., 1980, Astron. Nachr., 301, 95
Schatzman E., 1962, Ann. Astrophys., 25, 18
Schmitt J., Golub L., Harnden F., Jr, Maxson C., Rosner R., Vaiana G., 1985, ApJ, 290, 307
Schrijver C., 1987, in Linsky J. L., Stencel R. E., eds, Cool Stars, Stellar Systems, and the Sun. Lecture Notes in Physics, Vol. 291. Springer, Berlin, p. 135
Schrijver C., Dobson A. K., Radick R. R., 1989, ApJ, 341, 1035
Schussler M., 1975, A&A, 38, 263
Schwarzschild M., 1950, ApJ, 112, 222
Semel M., 1989, A&A, 225, 456
Semel M., Li J., 1996, Sol. Phys., 164, 417
Semel M., Donati J.-F., Rees D., 1993, A&A, 278, 231
Semel M., Vélez J. R., González M. M., Ramos A. A., Stift M., Ariste A. L., Leone F., 2009, A&A, 504, 1003
Shultz M. et al., 2019, MNRAS, 490, 4154
Shulyak D., Ryabchikova T., Kochukhov O., 2013, A&A, 551, A14
Sikora J., Wade G., Power J., Neiner C., 2018, MNRAS, 483, 2300
Silvester J., Wade G., Kochukhov O., Bagnulo S., Folsom C., Hanes D., 2012, MNRAS, 426, 1003
Simon T., Fekel F. C., Jr, 1987, ApJ, 316, 434
Skumanich A., 1972, ApJ, 171, 565
Slovak M., Barnes T., 2002, Bull. Am. Astron. Soc., 34, 655
Snik F., Jeffers S., Keller C., Piskunov N., Kochukhov O., Valenti J., Johns-Krull C., 2008, in McLean I. S., Casali M, eds, Proc. SPIE Conf. Ser. Vol. 7014, Ground-based and Airborne Instrumentation for Astronomy II. SPIE, Bellingham, p. 70140O
Solanki S. K., 1993, Space Sci. Rev., 63, 1
Soubiran C., Le Campion J.-F., De Strobel G. C., Caillo A., 2010, A&A, 515, A111
Soubiran C. et al., 2018, A&A, 616, A7
Spitzer L. J., 1958, in Lehnert B., ed., Electromagnetic Phenomena in Cosmical Physics, Vol. 6. Cambridge Univ. Press, Cambridge, p. 169
Spruit H., 2002, A&A, 381, 923
Stenflo J., 1985, in de Jager C., Svestka Z., eds, Progress in Solar Physics. Springer, Berlin, p. 189
Stenflo J. O., 1989, A&AR, 1, 3
Stix M., 1982, in Fricke W., Teleki G., eds, Sun and Planetary System. Astrophysics and Space Science Library, Vol. 96. Springer, Berlin, p. 63
Strassmeier K. G., Fekel F. C., Bopp B. W., Dempsey R. C., Henry G. W., 1990, ApJS, 72, 191
Struve O., 1875, MNRAS, 35, 367
Suchkov A. A., Makarov V. V., Voges W., 2003, ApJ, 595, 1206
Takeda G., Ford E. B., Sills A., Rasio F. A., Fischer D. A., Valenti J. A., 2007, ApJS, 168, 297
Tokovinin A., 2014, AJ, 147, 87
Tokovinin A., Lépine S., 2012, AJ, 144, 102
Toner C., Gray D. F., 1988, ApJ, 334, 1008
Torres G., Andersen J., Giménez A., 2010, A&AR, 18, 67
Trilling D. E. et al., 2007, ApJ, 658, 1289
Trust O., Jurua E., De Cat P., Joshi S., 2020, MNRAS, 492, 3143
Uitenbroek H., 2003, ApJ, 592, 1225

Ulmschneider P., Priest E., Rosner R., 1991, Mechanisms of Chromospheric and Coronal Heating: Proceedings of the International Conference, Heidelberg, June 1990. Springer, Berlin Heidelberg
Vaughan A. H., Preston G. W., Wilson O. C., 1978, PASP, 90, 267
Vican L., 2012, AJ, 143, 135
Voges W. et al., 1999, A&A, 349, 389
Wade G., Donati J.-F., Landstreet J., Shorlin S., 2000, MNRAS, 313, 851
Wade G. A. et al., 2016, MNRAS, 456, 2
Walter F. M., Matthews L. D., Linsky J. L., 1995, ApJ, 447, 353
Watson C. L., Henden A, Price A, 2006, The Society for Astronomical Sciences 25th Annual Symposium on Telescope Science, 25, p. 47
Weber E. J., Davis L., Jr, 1967, ApJ, 148, 217
Wenger M. et al., 2000, A&AS, 143, 9
Wilson E. B., 1927, JASA, 22, 209
Wilson O., 1966, ApJ, 144, 695
Wilson O., 1978, ApJ, 226, 379
Wolff S. C., Wolff R. J., 1970, ApJ, 160, 1049
Wolff S. C., Heasley J. N., Varsik J., 1985, PASP, 97, 707
Worley C. E., Heintz W. D., 1983, PUSNO, 24, 1
Wright C. O., Egan M. P., Kraemer K. E., Price S. D., 2003, AJ, 125, 359
Wright J. T., Marcy G. W., Butler R. P., Vogt S. S., 2004, ApJS, 152, 261
Zeldovich I. B., Ruzmaikin A. A., Sokolov D. D., 1983, Magnetic Fields in Astrophysics. Gordon and Breach, New York

APPENDIX A: NOTES ON INDIVIDUAL STARS

Below is background information and summary of the results for individual 25 transition project stars. Information on the 31 BRITEpol stars used in this paper can be found in Marsden et al. (in preparation). We estimated the rotational period of our stars using literature values for $v \sin i$, stellar radius, and assuming an inclination of 60 deg.

A1 σ Boo

σ Boo (HIP 71284) is a young triple star system with component V magnitudes 4.50, 10.66, 12.08, respectively (Mason et al. 2001). Component B was separated from the primary by 215 arcsec in 2012 and component C by 222 arcsec in 2002 based on data from the continuously updated Washington Double Star Catalogue (Mason et al. 2001). σ Boo is classified as a standard F2V star in the MK classification system Johnson & Morgan (), while Samus et al. (2017) classify it as F3V. Hoffleit (1991) suggests σ Boo is possibly a δ Scuti type variable, although Chang et al. (2013) did not include it in a recent catalogue of 1578 δ Scuti variables.

We obtained fourteen polarized spectra for σ Boo over a 2.6 h interval on 2017 January 14 corresponding to 1.5 per cent of the estimated rotational period of 6.8 d. The mean LSD profile (Fig. B2) combined 6304 lines, and a magnetic detection was obtained from the mean LSD Stokes V profile. We estimated B_l at -1.4 ± 0.4 G. Our radial velocity determination $+0.28 \pm 0.01$ km s^{-1} (Table 5) is similar to the value of $+0.37 \pm 0.09$ km s^{-1} in Anderson & Francis (2012), and our S-index 0.240 ± 0.004 (Table 5) is within the range 0.156–0.253 from Pace (2013).

A2 ϵ Lib

ϵ Lib (HIP 75379) is a single-lined spectroscopic binary (Tokovinin 2014) first observed by Campbell (1899). The system consists of spectral types F4V (Abt 2009) and K5-M2 (Castelaz 1989) with an orbital period of 229 d (Malkov et al. 2012). The secondary is unresolved by interferometry (Hartkopf, McAlister & Franz 1989).

We obtained fourteen polarized spectra for ϵ Lib over a 3.5 h interval on 2017 March 13, corresponding to 2.2 per cent of the estimated rotational period of 12.7 d. The mean LSD profile (Fig. B3) combined 6829 lines, and shows a magnetic detection. We estimated B_l at -0.5 ± 0.1 G, based on the mean LSD. Our radial velocity determination -13.98 ± 0.70 km s^{-1} (Table 5) is larger than the value of -9.8 ± 0.7 km s^{-1} in Anderson & Francis (2012). We determined an S-index of 0.180 ± 0.012 (Table 5) and this is the first value in the literature.

A3 ϵ Cet

ϵ Cet (HIP 12390) is a spectroscopic binary (Eggleton, Pringle & Division 1985; Duquennoy & Mayor 1988), consisting of F5V+F6V components (Fuhrmann 2008) with a short orbital period of 2.62 yr (Finsen 1955). The system was described as astrometrically, photometrically, and spectroscopically elusive by Fuhrmann (2008) with the stars being difficult to separate. Early radial velocity measurements of ϵ Cet were useless due to scatter caused by blending of two components of nearly equal brightness (Duquennoy & Mayor 1988). This was due to the high rotational velocity of one of the components, combined with a maximum Doppler displacement of 15 kms^{-1} (Duquennoy & Mayor 1988). The spectra of ϵ Cet are mostly not able to be individually separated, and the use of assumptions are required to untangle them (Docobo & Andrade 2013). The angular separation of the components was 0.1 arcsec in 2015 (Mason et al. 2001).

We obtained sixteen polarized spectra for ϵ Cet over a 6.0 h interval on 2016 September 21, corresponding to 2.5 per cent of the estimated rotational period of 10.2 d. The mean LSD profile (Fig. B4) combined 6693 lines, and a magnetic detection was obtained from the mean LSD Stokes V profile. We are unable to determine whether the magnetic detection was on the F5V or F6V components because the two stars could not be separated spectroscopically. We estimated B_l at $+0.6 \pm 0.1$ G. Our radial velocity determination $+15.81 \pm 0.26$ km s^{-1} (Table 5) is similar to the value of $+15.49 \pm 0.19$ km s^{-1} in Anderson & Francis (2012), and our S-index 0.186 ± 0.003 (Table 5) was less than 0.219 in Pace (2013).

A4 α Com

α Com (HIP 64241) is a triple star consisting of a double-lined spectroscopic binary (Duquennoy, Mayor & Halbwachs 1991) of F5V and F6V components (Edwards 1976; Soubiran et al. 2018), and a V magnitude 10.2 component with an angular separation of 85 arcsec in 2014 based on data from the continuously updated Washington Double Star Catalogue (WDS) (Mason et al. 2001). The system was first observed by Struve (1875) who reported that occultations were observed (Muterspaugh et al. 2015). Roman (1950) describes α Com as a close visual binary, with equal F5 components, and showing weak lines. Hartkopf et al. (1989) describes α Com as a 'lovely edge-on system' with an orbital inclination close to 90 deg, and suggested a partial eclipse was possibly missed in early 1990. The eclipsing binary has the third longest period known ($P = 25.85$ yr) (Lipunov et al. 2016), with only eight eclipsing stars having periods longer than 10 yr.

We obtained twenty-seven polarized spectra for α Com over a 3.8 h interval on 2017 February 16, corresponding to 5.3 per cent of the estimated rotational period of 3.0 d. The mean LSD profile (Fig. B5) combined 7628 lines, and a magnetic detection is visible in the Stokes V profile. We are unable to determine whether the magnetic detection was on the F5V or F6V components because the two stars could not be separated spectroscopically.

We estimated B_l at $+3.1 \pm 0.3$ G. Our radial velocity determination -18.02 ± 0.27 km s^{-1} (Table 5) is larger the value of -16.05 ± 0.21 km s^{-1} in Anderson & Francis (2012), and our S-index 0.272 ± 0.008 (Table 5) is smaller than the 0.308 in Pace (2013).

A5 ω Dra

ω Dra (HIP 86201) is a triple star system consisting of double-lined spectroscopic binary (Abt & Levy 1976; Konacki et al. 2010), and a V magnitude 13.2 common proper motion companion with an angular separation of 70 arcsec (Abt & Levy 1976; Fekel, Tomkin & Williamson 2009). The mases of the primary component are 1.46 $M_\odot$ and secondary 1.18 $M_\odot$ (Konacki et al. 2010), which corresponds to spectral types F2V and F8V, respectively. The two F-stars have an orbital period of 5.28 d, with a nearly face-on ($i = 151$ deg), circular orbit ($e = 0.00220$) (Konacki et al. 2010).

We obtained sixteen polarized spectra for ω Dra over a 3.6 h interval on 2017 May 5, corresponding to 1.5 per cent of the estimated rotational period of 10.1 d. The spectral lines of two F-stars had a relatively wide separation which enabled us to run LSD analysis and FAP for the two components separately. The F2V star did not show a magnetic detection, while a magnetic field was detected on the F8V component. The mean LSD profile (Fig. B6) for the F8V star combined 9099 lines and a strong signal is visible in the Stokes V profile. We estimated B_l for the F8V component at -2.9 ± 1.2 G and the F2V component $+0.2 \pm 0.1$ G. Our radial velocity determination for the F2V was -47.74 ± 0.71 km s^{-1}, and the F8V $+28.42 \pm 0.89$ km s^{-1} (Table 5). Our S-index estimation for the F2V component was 0.240 ± 0.007 and for the F8V 0.307 ± 0.008 (Table 5) which were both greater than the range of 0.174–0.191 from Pace (2013).

A6 h Dra

h Dra (HIP 82860) is a single-lined spectroscopic binary consisting of F8V and M1V components (Abt 2009). The faint companion orbits with a period of 52.1 d (Abt & Levy 1976) and has an estimated mass of 0.54 $M_\odot$ assuming it is a main-sequence star (Behr et al. 2009). The Yale Bright Star Catalogue (Hoffleit 1991) lists h Dra as a possible δ Scuti-type variable with a V magnitude range of 4.85–4.91, and the star shows an excess emission in the infrared, indicating a possible debris disc (Cotten & Song 2016).

We obtained sixteen polarized spectra for h Dra over a 3.7 h interval on 2017 May 9, corresponding to 1.8 per cent of the estimated rotational period of 6.0 d. The mean LSD profile (Fig. B7) combined 7168 lines, and a strong magnetic detection is visible in the Stokes V profile. We estimated B_l at $+8.3 \pm 0.9$ G. Our radial velocity determination -32.95 ± 0.03 km s^{-1} (Table 5) is larger than the value of -21.00 ± 0.80 km s^{-1} in Anderson & Francis (2012), and our S-index 0.251 ± 0.036 (Table 5) is greater than the range 0.195–0.219 given in Pace (2013).

A7 36 UMa

36 UMa (HIP 51459) is a multiple star system with high proper motion (Wenger et al. 2000). Component A is an F8V star with V magnitude 4.9, forming a wide binary, with an estimated separation of 123 arcsec from the spectroscopic binary BC in 2016, based on data from the continuously updated WDS (Mason et al. 2001). We obtained twelve polarized spectra for 36 UMa over a 2.6 h interval on 2017 January 13, corresponding to 1.2 per cent of the estimated rotational period of 8.2 d. The mean LSD profile (Fig. B8) combined 7058 lines, and showed a magnetic detection. We estimated B_l at -0.3 ± 0.1 G. Our radial velocity determination 8.71 ± 0.01 km s^{-1} (Table 5) is close to the value of 8.69 ± 0.09 km s^{-1} in Anderson & Francis (2012), and our S-index 0.193 ± 0.011 (Table 5) is close to the range of 0.193 to 0.203 given in Pace (2013) in 1978 December and May.

A8 17 Crt

17 Crt (HIP 56280) is a visual double star consisting of two F8V components (Gray, Napier & Winkler 2001) separated by 9.7 arcsec in 2012, based on data from the continuously updated Washington Double Star Catalogue (Mason et al. 2001). We obtained eighteen polarized spectra for 17 Crt A over a 4.4 h interval on 2017 March 5, corresponding to 1.9 per cent of the estimated rotational period of 10.0 d. The mean LSD profile (Fig. B9) combined 8309 lines, and shows a magnetic detection. We estimated B_l at $+0.4 \pm 0.1$ G. Our radial velocity determination $+5.85 \pm 0.01$ km s^{-1} (Table 5) is close to the value of $+5.80 \pm 0.40$ km s^{-1} in Anderson & Francis (2012), and our S-index 0.157 ± 0.013 (Table 5) is lower than the range 0.158–0.167 given in Pace (2013).

A9 γ CrA

γ CrA (HIP 93825) is a close visual double star of equal mass F8V components (Heintz 1986). Components AB have an orbital period of approximately 120 yr (Evans, Menzies & Stoy 1957) and an estimated angular separation of 1.4 arcsec in 2017 based on data from the continuously updated Washington Double Star Catalogue (Mason et al. 2001). According to Raghavan et al. (2010) there is another unresolved companion implied by proper motion acceleration.

We obtained 12 spectra of γ CrA (component B) over a 1.5 h interval on 2017 June 6, corresponding to 0.5 per cent of the estimated rotation period of 12.6 d. Component A was observed on 2017 June 7 and showed no magnetic detection (B_l estimated at -0.1 ± 0.1 G), based on an LSD profile of 14 spectra and 7613 lines. We detected a magnetic field on component B using the mean LSD (Fig. B10) of 12 spectra and combining 7608 lines. We estimated B_l at $+5.6 \pm 0.8$ G. Our radial velocity determination of -52.82 ± 0.06 km s^{-1} (Table 5) was similar to the value of -51.60 ± 0.30 km s^{-1} from Anderson & Francis (2012), and our S-index 0.139 ± 0.015 (Table 5) was smaller than 0.165 found in Pace (2013).

A10 τ Psa

τ Psa (HIP 109422) is a single, high proper motion, F6V star (Wenger et al. 2000) with close to solar metallicity (Soubiran et al. 2010). It has a theoretical stellar convection zone mass of 0.002 $M_\odot$ and convection zone depth of 0.236 $M_\odot$ (Takeda et al. 2007). τ Psa has been identified as a potential candidate to host a debris-disc, as shown by emission of an infrared excess (Ertel et al. 2016). We obtained fourteen polarized spectra for τ Psa over a 4.3 h interval on 2016 October 15, corresponding to 3.5 per cent of the estimated rotational period of 5.1 d. The mean LSD profile (Fig. B11) combined 8637 lines, and a marginal magnetic detection was obtained from the mean LSD Stokes V profile. We estimated B_l at -0.6 ± 0.2 G. Our radial velocity determination -16.11 ± 0.01 km s^{-1} (Table 5) is similar to the value of -16.23 ± 0.09 km s^{-1} in Anderson &

Francis (2012), and our S-index 0.156 ± 0.011 (Table 5) is in the range of 0.144–0.173 from Pace (2013).

A11 10 UMa

10 UMa (HIP 44248) is a multiple star system, previously located in the constellation Ursa Major, but now included in boundaries of Lynx (Griffin 1999). The system is moving as part of the Hyades stream (Eggen 1960) with a high proper motion (Wenger et al. 2000). The primary component is spectral type F3V, and the secondary component G5V (Montesinos et al. 2016). Components AB form a double-lined spectroscopic binary (Muterspaugh et al. 2010) with *V* magnitudes 4.18 and 6.18, respectively (Mason et al. 2001). Components AB,C form an optical binary with *V* magnitudes 4.03, 10.06, respectively (Mason et al. 2001). Components AB have an orbital period of 21.8 yr, and angular separation of 0.4 arcsec in 2016, according to the continuously updated WDS (Mason et al. 2001). The *ROSAT* All-Sky Survey Bright Source Catalogue lists 10 UMa as an X-Ray source (Voges et al. 1999), although it was not clear if this was due to the F-type primary, or G-type secondary star.

We obtained twenty-one polarized spectra for 10 UMa over a 3.6 h interval on 2016 December 22, corresponding to 3.4 per cent of the estimated rotational period of 3.9 d. The LSD profile combined 8930 lines and a definite magnetic detection was obtained from the mean Stokes *V* LSD profile. The magnetic signature visible in the Stokes *V* profile is aligned with the narrow-lined component of the Stokes *I* profile. The detection is therefore most likely due to the slower rotating (narrower lined) G5V component. We estimated B_l of 10 UMa at −4.8 ± 1.1 G, is consistent with Marsden et al. (2014) who determined B_l of 3.2 G for G-type stars.

The spectral line analysis and S-index estimation were completed on the blended spectral line, therefore contain a mix from the F3V and G5V components. Our calculated radial velocity of +27.68 ± 0.04 km s^{-1} is similar to the value of +27.80 ± 2.80 km s^{-1} in Anderson & Francis (2012). Our S-index 0.216 ± 0.007 (Table 5) is in the range of values 0.206–0.233 found in Buccino & Mauas (2008). The S-index contrasts with a survey of chromospheric activity by Martinez-Arnaiz et al. (2010) which listed 10 UMa as inactive.

A12 σ Cet

σ Cet (HIP 11783) was first identified as a triple star by McLaughlin (1947). Components AB form a wide binary (separation 346 arcsec in 1999) with common proper motion, and *V* magnitudes of 4.79, 8.77, respectively (Mason et al. 2001), and spectral types F5V+K2.5V (Tokovinin & Lépine 2012). Component A is a spectroscopic binary with component *V* magnitudes 4.75 and 10.08 (Tokovinin 2014). Glass (1974) identified σ Cet as a Southern hemisphere standard star for JHKL photometry. σ Cet belongs to a class of older F-type stars identified by Suchkov, Makarov & Voges (2003) which show X-ray emission.

We obtained seven polarized spectra for σ Cet over a 1.5 h interval on 2016 September 20, corresponding to 0.5 per cent of the estimated rotational period of 12.1 d. The mean LSD profile combined 7482 lines, and did not show a magnetic detection. We estimated B_l at 0.0 ± 0.2 G. Our radial velocity determination −29.80 ± 0.01 km s^{-1} (Table 5) is the similar to −27.50 ± 0.90 km s^{-1} in Anderson & Francis (2012). Our S-index 0.160 ± 0.001 (Table 5) is within the range of 0.157–0.197 in Pace (2013).

A13 58 Oph

58 Oph (HIP 86736) is a high proper-motion star which was classified as a standard star by Cousins (1971). It is a possible double star system whose binary nature may have been detected a visual grazing occultation of the moon in 1975 (Hoffleit 1991), however, the binary nature of 58 Oph is elusive, with a lunar occultation in 2011 failing to resolve the stellar system (Herald et al. 2016). Mason et al. (2001) lists the primary star as F5V, *V* magnitude 5.1, and the secondary with a *V* magnitude 6.90 corresponding to a spectral type of G5.

We obtained thirteen polarized spectra for 58 Oph over a 2.8 h interval on 2017 May 12, corresponding to 2.4 per cent of the estimated rotational period of 4.7 d. The mean LSD profile combined 6833 lines, and did not show a magnetic detection with an estimated B_l of +0.4 ± 0.2 G. Our radial velocity determination +10.34 ± 0.01 km s^{-1} (Table 5) is the similar to +10.20 km s^{-1} in Anderson & Francis (2012). Our S-index 0.164 ± 0.018 (Table 5) is less than 0.197 in Pace (2013).

A14 ψ Peg

ψ Peg (HIP 112447) is a relatively nearby (16 pc), high proper motion multiple star system. ψ Peg consists of a F6V (4.20 mag) primary (Wenger et al. 2000), and M1V (11.10 mag) secondary (Fracassini et al. 2001). The angular separation of components AB was 11.0 arcsec in 2015 (Mason et al. 2001). The General Catalogue of Variable Stars (Samus et al. 2017) lists ψ Peg as a variable with an amplitude of 0.02. We obtained ten polarized spectra for ψ Peg over a 1.4 h interval on 2016 August 15, corresponding to 0.7 per cent of the estimated rotational period of 9.5 d. The mean LSD profile combined 7499 lines, and did not show a magnetic detection. We estimated B_l at +0.1 ± 0.1 G. Our radial velocity determination −5.73 ± 0.01 km s^{-1} (Table 5) is similar to −5.37 ± 0.08 km s^{-1} in Anderson & Francis (2012). Our S-index 0.148 ± 0.001 (Table 5) is within the range of values 0.121–0.176 from 2002 to 2008 (Isaacson & Fischer 2010).

A15 μ Cyg

μ Cyg (HIP 107310) is a multiple star system with components AB forming an optical double, 1.8 arcsec separation in 2016 (Mason et al. 2001) and spectral type F6V+G2V (Hoffleit 1991). Component AB V magnitudes are 4.75 and 6.18 (Wenger et al. 2000) with an orbital period determined as 507.5 yr (Worley & Heintz 1983) or 840 yr (Fuhrmann 2008). We obtained fifteen polarized spectra for μ Cyg over a 2.8 h interval on 2016 August 12, corresponding to 0.9 per cent of the estimated rotational period of 12.8 d. The mean LSD profile combined 7043 lines, and did not show a magnetic detection. We estimated B_l at −0.4 ± 0.1 G. Our radial velocity determination +16.97 ± 0.02 km s^{-1} (Table 5) is the same as +16.95 ± 0.16 km s^{-1} in Anderson & Francis (2012). Our S-index 0.178 ± 0.001 (Table 5) is greater than the values 0.160 in 1981 and 0.155 in 1982 (Duncan et al. 1991).

A16 ι Psc

ι Psc (HIP 116771) is a triple star system with component V magnitudes 4.18, 14.10, and 12.51 (Mason et al. 2001). Components AB form an optical double (Hoffleit 1991) with an angular separation of 123 arcsec in 2008 (Mason et al. 2001). The International Variable Star Index (Watson 2006) lists ι Psc as a variable star with a small magnitude range of 4.11–4.14, while Johnson & Morgan (1953) list 20 Oph as a F7V standard star. The star is sharp-lined, with an overabundance of rare-earth elements (Rice & Hill 1988), while containing overall abundances less than solar (Adelman et al. 1991). The sharp spectral lines has enabled the star to be used as a radial velocity standard star (Cakirli, İbanoğlu & Frasca 2007). We obtained fourteen polarized spectra for ι Psc over a 2.0 h interval on 2016 August 16, corresponding to 1.2 per cent of the estimated rotational period of 10.5 d. The mean LSD profile combined 7502 lines, and did not show a magnetic detection. We estimated B_l at -0.2 ± 0.1 G. Our radial velocity determination $+5.77 \pm 0.01$ km s^{-1} (Table 5) was close to the value of $+5.95 \pm 0.08$ km s^{-1} in Anderson & Francis (2012). Our S-index 0.161 ± 0.001 (Table 5) is consistent with values of 0.152 in 1984, and 0.170 in 1990 (Buccino & Mauas 2008).

A17 σ02 UMa

σ02 UMa (HIP 45038) is a triple star system with V magnitudes 4.87, 8.85, and 10.32 (Mason et al. 2001). Component AB spectral types are F7IV-V+K2V Hoffleit (1991), and separated by 4.3 arscec in 2016 (Mason et al. 2001). The orbital period of AB is approximately 1500 yr (Scardia 1980). We obtained seven polarized spectra for σ02 Uma over a 2.0 h interval on 2016 December 21–22, corresponding to 0.8 per cent of the estimated rotational period of 11.0 d. The mean LSD profile combined 8648 lines, and did not show a magnetic detection. We estimated B_l at $+0.1 \pm 0.1$ G. Our radial velocity determination -3.13 ± 0.01 km s^{-1} was close to the value of -2.98 ± 0.09 km s^{-1} in Anderson & Francis (2012), and our S-index of 0.135 ± 0.014 (Table 5) was lower than the range 0.138–0.171 from Pace (2013).

A18 δ Equ

δ Equ (HIP 104858) is a well-known visual and spectroscopic binary which has been studied since the first observations by Herschel in the 1880's (Muterspaugh et al. 2005). The binary consists of F7V and G0V components (Wenger et al. 2000), with V magnitudes 5.2 and 5.3 (Hoffleit 1991). The components have an orbital period of 5.7 yr (Malkov et al. 2012) and were estimated to be separated by 0.3 arcsec in 2017 based on data from the continuously updated WDS (Mason et al. 2001). Components AB have nearly identical mass of 1.192 $M_\odot$ and 1.187 $M_\odot$ (Muterspaugh et al. 2008). δ Equ is a useful star for binary studies because it is bright, relatively close (18 pc), and contains a semimajor axis of 0".05. According to Muterspaugh et al. (2005) these features, accompanied by its short orbital period, means that it can be studied both visually and spectroscopically in a short period of time.

We obtained twelve polarized spectra for δ Equ over a 2.3 h interval on 2017 June 6, corresponding to 0.9 per cent of the estimated rotational period of 10.9 d. The mean LSD profile combined 7182 lines, and did not show a magnetic detection. We estimated B_l at $+0.7 \pm 0.2$ G. Our radial velocity determination -15.76 ± 0.05 km s^{-1} (Table 5) was close to the value of -15.85 ± 0.07 km s^{-1} in Anderson & Francis (2012), and our S-index 0.166 ± 0.016 (Table 5) was close to the value of 0.160 from Pace (2013).

A19 6 Cet

6 Cet (HIP 910) is a high proper motion single star used as a radial velocity standard (Gray 1982). It has a wide variety of spectral types quoted in the literature from F5 to F8, with Wenger et al. (2000) listing F8V. We obtained five polarized spectra for 6 Cet over a 1.0 h interval on 2017 August 10, corresponding to 0.3 per cent of the estimated rotational period of 13.1 d. The mean LSD profile combined 7659 lines, and did not show a magnetic detection. We estimated B_l at 0.0 ± 0.1 G. Our radial velocity determination $+15.14 \pm 0.01$ km s^{-1} (Table 5) was close to the value of $+14.81 \pm 0.09$ km s^{-1} in Anderson & Francis (2012), and our S-index 0.174 ± 0.001 (Table 5) is within the range of 0.136–0.180 given in Pace (2013).

A20 ζ Cnc

ζ Cnc (HIP 40167) is one of the best-known multiple star systems in the sky, first identified as a double by Mayer in 1756, and up to five components identified by lunar occultation in 1998 (Griffin 2000). Components A and B form a close visual pair with an angular separation of 1.2 arcsec in 2016 (Mason et al. 2001), and an orbital period of 59.7 yr (Gasteyer 1954). The spectral types of components AB are F8V and G0V (Wenger et al. 2000). As with many multiple star systems, there is some confusion in the literature about the naming of individual components. A comprehensive review of ζ Cnc by Griffin (2000) provides clarification on the naming the components.

We obtained three polarized spectra for ζ Cnc A over an 0.3 h interval on 2017 February 15, corresponding to 0.06 per cent of the estimated rotational period of 20.6 d. The mean LSD profile combined 8813 lines, and did not show a magnetic detection. We estimated B_l at -0.7 ± 0.4 G. Our radial velocity determination -5.24 ± 0.01 km s^{-1} (Table 5) was smaller than the value of -7.93 ± 0.08 km s^{-1} in Anderson & Francis (2012), and our S-index 0.143 ± 0.002 (Table 5) smaller than 0.160 in Pace (2013).

A21 HD 84117

HD 84117 (HIP 47592) is single, nearby, Sun-like star (O'Toole et al. 2009), with a spectral type F9V (Wenger et al. 2000). It exhibits solar-type metallicity ([Fe/H] −0.07), however is deficient in Mn, and enriched in Na and in elements of the s-process (Sr, Y, Zr, and Ba) (Da Silva et al. 2012). HD 84117 was a target for the Anglo-Australian Telescope rocky planet search (O'Toole et al. 2009), and showed a Doppler velocity variability which either indicated the star may contain multiple planets, or belong to a class of stars with unusual velocity variability. We obtained five spectra for HD 84117 over a 1.5 h interval on 2017 March 11, corresponding to 0.5 per cent of the estimated rotational period of 9.1 d. The mean LSD profile combined 8804 lines and did not show a magnetic detection. We estimated B_l at $+0.2 \pm 0.1$ G. Our radial velocity determination of $+34.80 \pm 0.01$ km s^{-1} (Table 5) was similar to the value of $+35.30 \pm 0.44$ km s^{-1} from (Anderson & Francis 2012), and our S-index 0.151 ± 0.006 (Table 5) is within the range of 0.147–0.186 between 2004 and 2009 (Pace 2013).

A22 κ Peg

κ Peg (HIP 107354) is a triple star system comprising components Ba,Bb,A (Docobo & Andrade 2013). The system departs from normal the naming convention by designating component B as the brightest. This has resulted in some confusion in naming in the literature. Spectral type of the components Ba,Bb,A are F5IV, G0V, F0IV, respectively (Docobo & Andrade 2013). Components AB orbit with a period of 11.5 yr, and components Ba,Bb have a short orbital period of 6 d (Behr et al. 2011). The V magnitudes of AB are 4.94 and 5.04 (Mason et al. 2001). The κ Peg system is difficult to observe (Barlow & Scarfe 1977) because of nearly equal magnitudes of the brightest two components, their small angular separation, high orbital inclination, and long orbital period.

We obtained thirty-four polarized spectra for κ Peg over a 5.3 h interval on 2016 August 16, corresponding to 2.4 per cent of the estimated rotational period of 9.0 d. It was difficult to disentangle the spectra, and it was not possible to determine which of the components had the magnetic detection. The mean LSD profile combined 6684 lines, and a magnetic detection was obtained from the mean LSD Stokes V profile. The Stokes V signal shows a double positive lobe, aligning with both the F5V and G0V components. We estimated B_l at $+0.9 \pm 0.3$ G. Our radial velocity determination -21.45 ± 2.62 km s^{-1} (Table 5) is different to the value of -0.80 ± 0.20 km s^{-1} in Anderson & Francis (2012) due to the binary nature of the system. Our S-index 0.237 ± 0.001 (Table 5) is greater than the value of 0.170 in Pace (2013).

A23 20 Oph

20 Oph (HIP 82369) is an high proper motion, spectroscopic binary consisting of F7V (Wenger et al. 2000) and a secondary later than G2V (Gomez & Abt 1982). Abt & Levy (1976) calculated an orbit of 3.5 yr from radial velocity measurements, however the secondary has never been detected with speckle interferometry (Gontcharov & Kiyaeva 2010). We obtained fifteen polarized spectra for 20 Oph over a 3 h interval on 2016 August 8, corresponding to 1.0 per cent of the estimated rotational period of 12.3 d. The mean LSD profile combined 8378 lines, and a magnetic detection was obtained from the mean LSD Stokes V profile. Due to the blended spectra it was not possible to say which component contained the magnetic detection. We estimated B_l at $+0.7 \pm 0.2$ G. Our radial velocity determination -0.30 ± 0.01 km s^{-1} (Table 5) is similar to the value of -1.60 ± 0.60 km s^{-1} in Anderson & Francis (2012), and our S-index 0.227 ± 0.001 (Table 5) is the only measurement in the literature.

APPENDIX B: LSD PROFILES FOR STARS WITH A MAGNETIC DETECTION

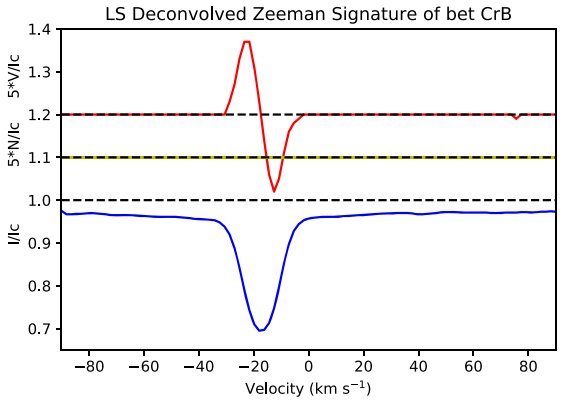

Figure B1. LSD profile (single spectra) for β CrB on 2017 April 23. The upper plot (red) shows the Stokes V profile (y-axis expanded and shifted up by 0.2 to allow better visibility). The middle plot (yellow) shows the null profile (expanded and shifted up by 0.1). The lower plot (blue) shows the Stokes I profile.

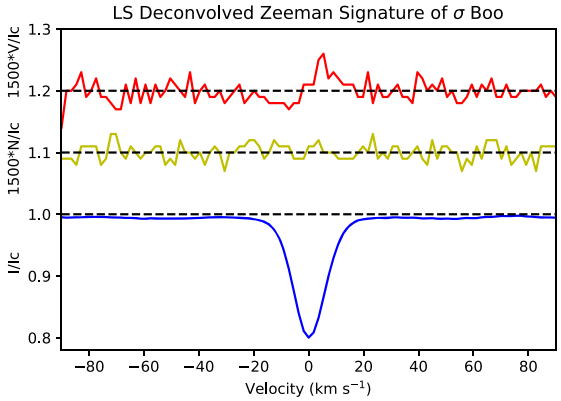

Figure B2. Mean LSD profile (combining 14 spectra) for σ Boo (F3V) on 2017 January 14. The plot is described in Fig. B1.

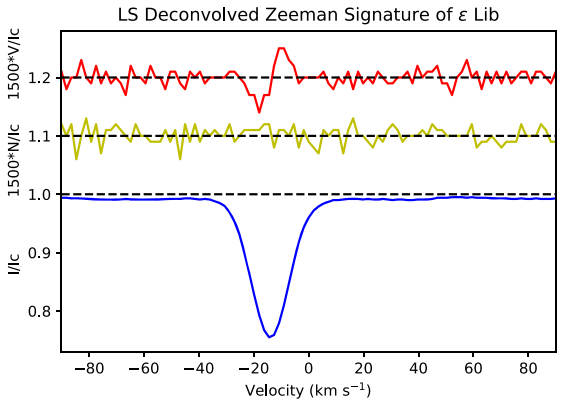

Figure B3. Mean LSD profile (combining 14 spectra) for ϵ Lib (F4V+K5-M2) on 2017 March 13. The plot is described in Fig. B1.

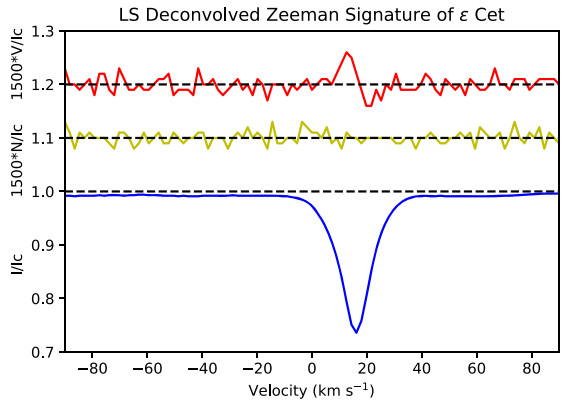

Figure B4. Mean LSD profile (combining 16 spectra) for ϵ Cet (F5V+F6V) on 2016 September 21. The plot is described in Fig. B1.

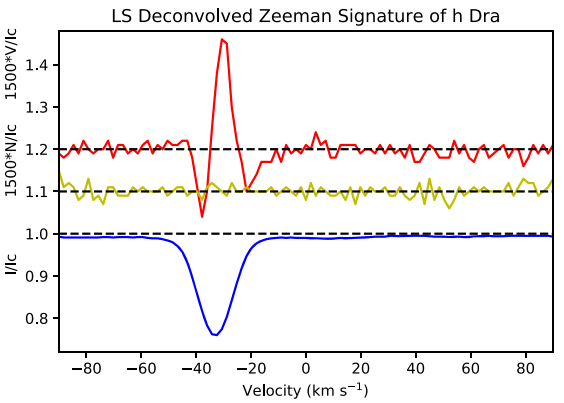

Figure B7. Mean LSD profile (combining 16 spectra) for h Dra (F8V+M1V) on 2017 May 9. The plot is described in Fig. B1.

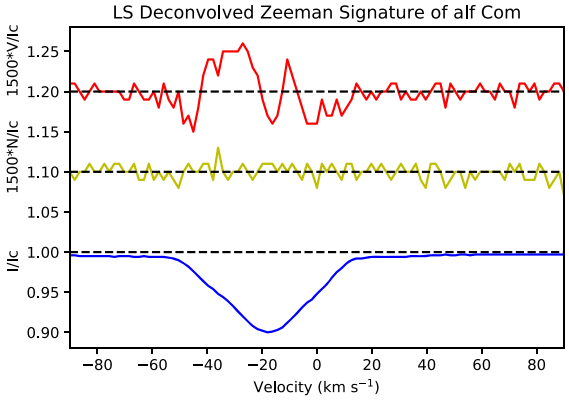

Figure B5. Mean LSD profile (combining 27 spectra) for α Com (F5V+F6V) on 2017 February 16. The plot is described in Fig. B1.

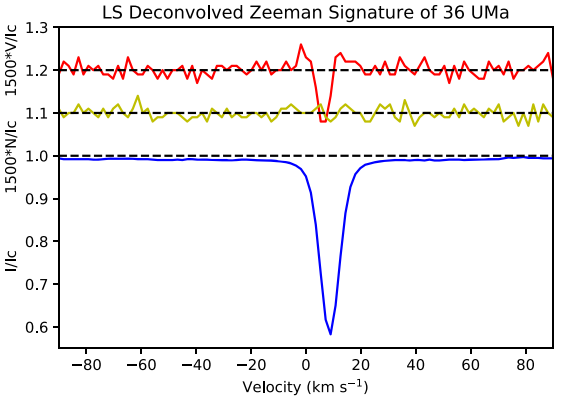

Figure B8. Mean LSD profile (combining 12 spectra) for 36 UMa (F8V+K7) on 2017 January 13. The plot is described in Fig. B1.

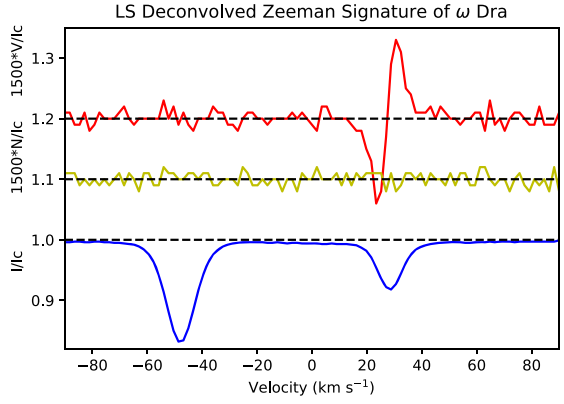

Figure B6. Mean LSD profile (combining 16 spectra) for ω Dra (F2V+F8V) on 2017 May 5. The F8 component with a definite magnetic signature is located at $+28.4\,\mathrm{km\,s^{-1}}$. The plot is described in Fig. B1.

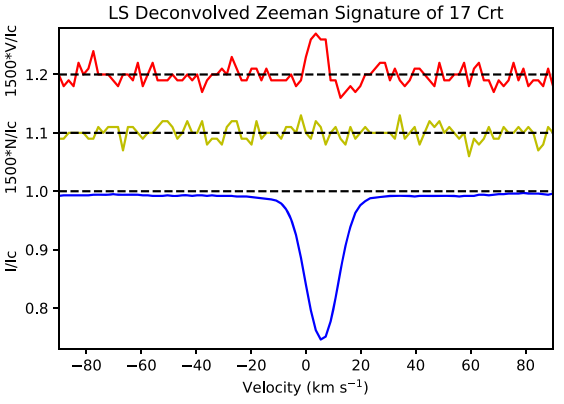

Figure B9. Mean LSD profile (combining 18 spectra) for 17 Crt (F8V+F8V) on 2017 March 5. The plot is described in Fig. B1.

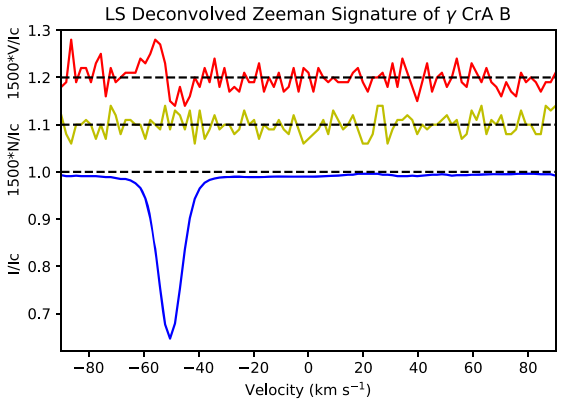

Figure B10. Mean LSD profile (combining 12 spectra) for γ CrA B (F8V) on 2017 June 6. The plot is described in Fig. B1.

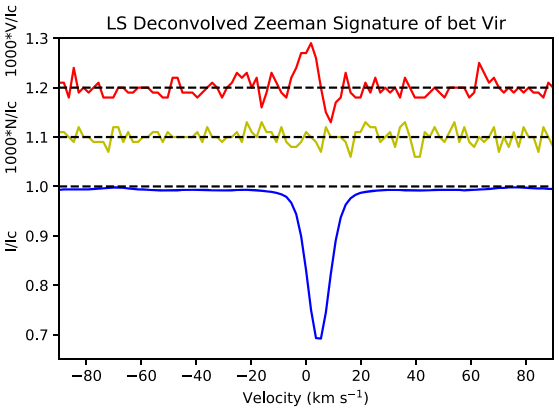

Figure B13. Mean LSD profile (combining two spectra) for β Vir (F9V) on 2017 April 11. The plot is described in Fig. B1.

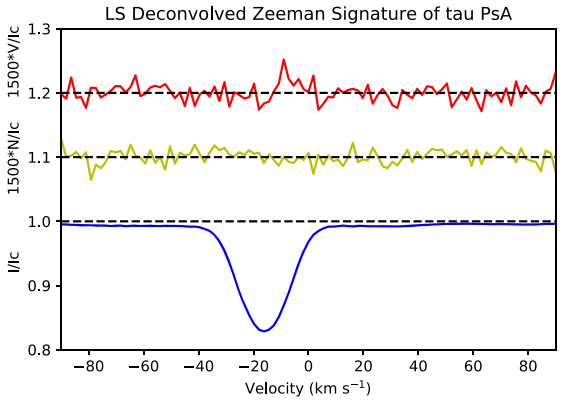

Figure B11. Mean LSD profile (combining 14 spectra) for τ PsA (F6V) on 2016 October 14. The plot is described in Fig. B1.

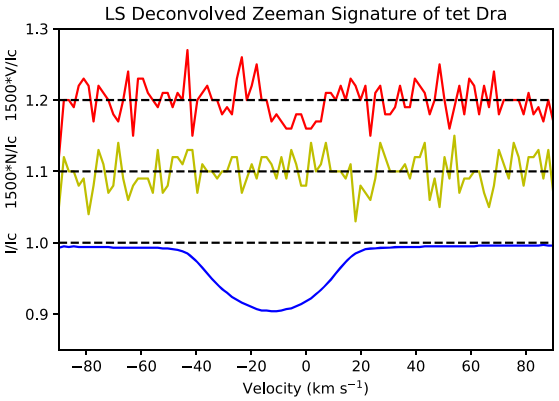

Figure B14. Mean LSD profile (combining three spectra) for θ Dra (F8IV+M2) on 24 April 2017. The plot is described in Fig. B1.

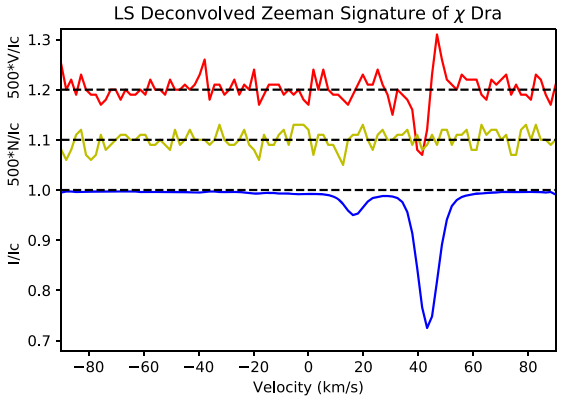

Figure B12. LSD profile (single spectra) for χ Dra (F7V+K1V) on 2015 April 24. The plot is described in Fig. B1.

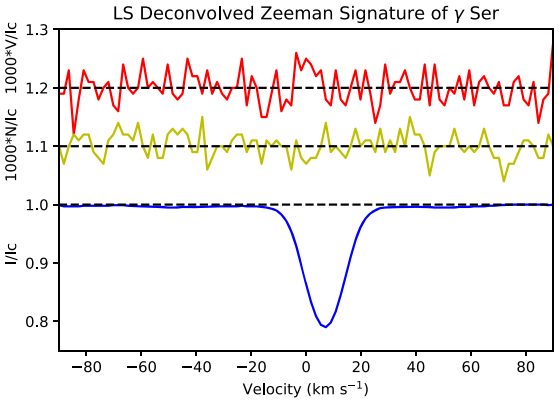

Figure B15. Mean LSD profile (combining two spectra) for γ Ser (F6V) on 2014 August 23. The plot is described in Fig. B1.

This paper has been typeset from a TEX/LATEX file prepared by the author.